

# Geochemistry, Geophysics, Geosystems

## RESEARCH ARTICLE

10.1029/2019GC008459

### Special Section:

Polar region geosystems

#### Key Points:

- Crustal thickness variations in the West Antarctic Rift System suggest along-strike variability in its Cenozoic evolution
- The lower crust and potentially the middle crust is positively radially anisotropic ( $V_{SH} > V_{SV}$ ) across West Antarctica
- The strongest positive crustal radial anisotropy is observed in the Haag-Ellsworth Whitmore Mountains block

#### Supporting Information:

- Supporting Information S1

#### Correspondence to:

J. P. O'Donnell,  
j.p.odonnell@leeds.ac.uk

#### Citation:

O'Donnell, J. P., Brisbourne, A. M., Stuart, G. W., Dunham, C. K., Yang, Y., Nield, G. A. et al. (2019). Mapping crustal shear wave velocity structure and radial anisotropy beneath West Antarctica using seismic ambient noise. *Geochemistry, Geophysics, Geosystems*, 20, 5014–5037. <https://doi.org/10.1029/2019GC008459>

Received 23 MAY 2019

Accepted 3 SEP 2019

Accepted article online 15 OCT 2019

Published online 14 NOV 2019

## Mapping Crustal Shear Wave Velocity Structure and Radial Anisotropy Beneath West Antarctica Using Seismic Ambient Noise

J. P. O'Donnell<sup>1</sup>, A. M. Brisbourne<sup>2</sup>, G. W. Stuart<sup>1</sup>, C. K. Dunham<sup>1</sup>, Y. Yang<sup>3</sup>, G. A. Nield<sup>4</sup>, P. L. Whitehouse<sup>4</sup>, A. A. Nyblade<sup>5</sup>, D. A. Wiens<sup>6</sup>, S. Anandkrishnan<sup>5</sup>, R. C. Aster<sup>7</sup>, A. D. Huerta<sup>8</sup>, A. J. Lloyd<sup>6</sup>, T. Wilson<sup>9</sup>, and J. P. Winberry<sup>8</sup>

<sup>1</sup>School of Earth and Environment, University of Leeds, Leeds, UK, <sup>2</sup>British Antarctic Survey, Natural Environment Research Council, Cambridge, UK, <sup>3</sup>Department of Earth and Planetary Science, Macquarie University, North Ryde, New South Wales, Australia, <sup>4</sup>Department of Geography, Durham University, Durham, UK, <sup>5</sup>Department of Geosciences, Pennsylvania State University, University Park, PA, USA, <sup>6</sup>Department of Earth and Planetary Sciences, Washington University, St. Louis, MO, USA, <sup>7</sup>Department of Geosciences, Colorado State University, Fort Collins, CO, USA, <sup>8</sup>Department of Geological Sciences, Central Washington University, Ellensburg, WA, USA, <sup>9</sup>School of Earth Sciences, Ohio State University, Columbus, OH, USA

**Abstract** Using 8- to 25-s-period Rayleigh and Love wave phase velocity dispersion data extracted from seismic ambient noise, we (i) model the 3-D shear wave velocity structure of the West Antarctic crust and (ii) map variations in crustal radial anisotropy. Enhanced regional resolution is offered by the UK Antarctic Seismic Network. In the West Antarctic Rift System (WARS), a ridge of crust ~26–30 km thick extending south from Marie Byrd Land separates domains of more extended crust (~22 km thick) in the Ross and Amundsen Sea Embayments, suggesting along-strike variability in the Cenozoic evolution of the WARS. The southern margin of the WARS is defined along the southern Transantarctic Mountains and Haag-Ellsworth Whitmore Mountains (HEW) block by a sharp crustal thickness gradient. Crust ~35–40 km is modeled beneath the Haag Nunataks-Ellsworth Mountains, decreasing to ~30–32 km thick beneath the Whitmore Mountains, reflecting distinct structural domains within the composite HEW block. Our analysis suggests that the lower crust and potentially the middle crust is positively radially anisotropic ( $V_{SH} > V_{SV}$ ) across West Antarctica. The strongest anisotropic signature is observed in the HEW block, emphasizing its unique provenance among West Antarctica's crustal units, and conceivably reflects a ~13-km-thick metasedimentary succession atop Precambrian metamorphic basement. Positive radial anisotropy in the WARS crust is consistent with observations in extensional settings and likely reflects the lattice-preferred orientation of minerals such as mica and amphibole by extensional deformation. Our observations support a contention that anisotropy may be ubiquitous in the continental crust.

**Plain Language Summary** The landmasses we recognize today as South America, Africa, Madagascar, India, Australia, and Antarctica were once joined in a supercontinent called Gondwana. West Antarctica is key to accurately recreating the Gondwana jigsaw puzzle, but the ice sheet limits access to the telling rock record. Here we map West Antarctica's crustal thickness using seismic waves to gauge where tectonic stretching has occurred. The thickest crust is found beneath the southern Transantarctic Mountains and Haag Nunataks-Ellsworth Mountains. Thinner crust characterizes the West Antarctic Rift System (WARS), being thinnest in the Ross and Amundsen Sea Embayments. The crustal thickness variations we map along the WARS suggest a complex history involving several rifting episodes since the Gondwana breakup. This can help inform Gondwana reconstructions. We also find that horizontally polarized seismic shear waves travel faster than vertically polarized shear waves (“positive radial anisotropy”) in the crust across West Antarctica. The strongest positive radial anisotropy is observed in the Haag-Ellsworth Whitmore Mountains block, emphasizing its unique provenance among West Antarctica's constituent crustal units. The observation of positive radial anisotropy in the WARS is typical of rifted crust and is probably caused by the alignment of minerals such as mica and amphibole during stretching.

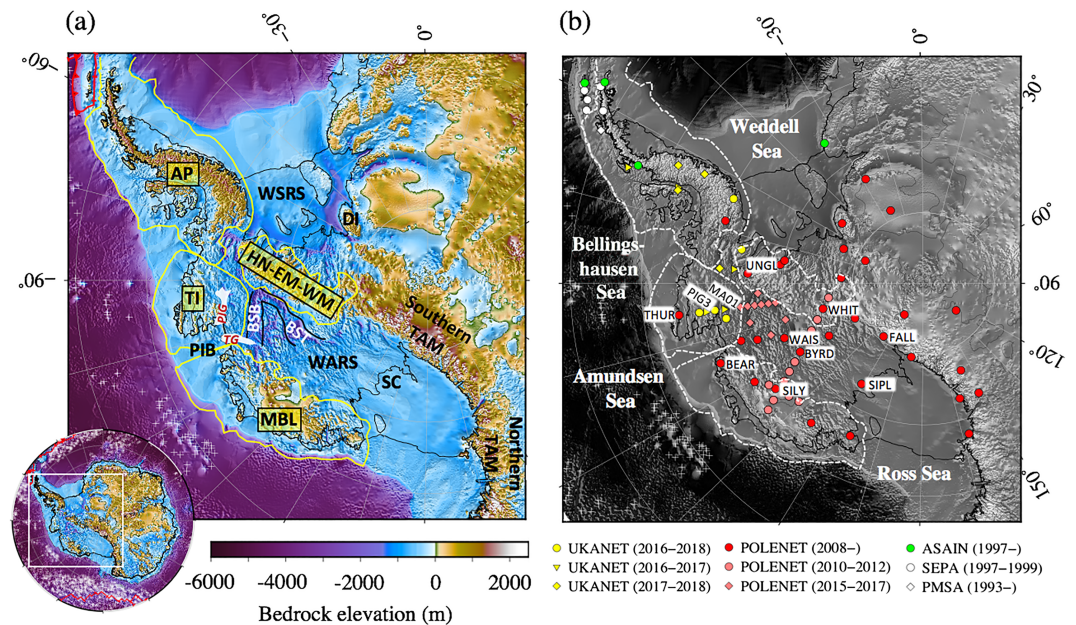


**Figure 1.** (a) Map of West Antarctic BEDMAP2 bedrock topography (Fretwell et al., 2013) annotated with tectonic boundaries. Following Dalziel and Elliot (1982), yellow lines delineate the major crustal blocks of West Antarctica that predate Gondwana fragmentation (AP, Antarctic Peninsula; TI, Thurston Island; MBL, Marie Byrd Land; HN-EM-WM, Haag-Ellsworth Whitmore Mountains block, hereafter HEW). The approximate locations of Pine Island Glacier (PIG) and Thwaites Glacier (TG) in the Amundsen Sea Embayment are outlined in white. Plate boundaries are marked in red, and white crosses show the locations of seamounts. Other abbreviated geographic features: BSB, Byrd Subglacial Basin; BST, Bentley Subglacial Trench; DI, Dufek Intrusion; PIB, Pine Island Bay; SC, Siple Coast; TAM, Transantarctic Mountains; WARS, West Antarctic Rift System; WSRS, Weddell Sea Rift System. (b) Map showing the location of the UK Antarctic Seismic Network, POLENET-ANET, ASAIN, SEPA and GSN seismic stations used in this study superimposed on grayscale bedrock topography. Specific stations referred to in the text are labeled. (For interpretation of the references to color in the figure(s), the reader is referred to the web version of this article). UKANET = UK Antarctic Seismic Network; ASAIN = Antarctic Seismographic Argentinean Italian Network; SEPA = Seismic Experiment in Patagonia and Antarctica.

## 1. Introduction

The West Antarctic Rift System (WARS; Figure 1) developed as a result of late Mesozoic and Cenozoic motion between East and West Antarctica and is one of the largest continental rift systems on Earth (e.g., Cande et al., 2000). Unravelling its tectonic history holds the key to global plate circuit closure (e.g., Müller et al., 2007). The major extensional phase in the WARS is inferred to have occurred in the Late Cretaceous between ~105 and 85 Ma (e.g., Divenere et al., 1996; Fitzgerald, 2002; Lawver & Gahagan, 1994). While Paleogene to Neogene extension in the western Ross Sea is supported by marine geophysical data (e.g., Cande et al., 2000; Davey et al., 2006; Granot & Dyment, 2018), the Cenozoic evolution of the eastern WARS (that portion approximately east of the Ross Ice Shelf) is subject to more speculation owing to the obscuring West Antarctic Ice Sheet (WAIS). Kinematic studies offer contrasting models of Cenozoic motion in the eastern WARS, ranging from implied uniform extension (Cande et al., 2000) to convergence (Davey et al., 2006) to dextral transcurrent motion (Müller et al., 2007). Most recently, Granot and Dyment (2018) modeled late Cenozoic extension in the western Ross Sea transitioning spatially to dextral transcurrent motion beneath the Ross Ice Shelf to oblique convergence beneath the WAIS.

In the eastern WARS where the ice cover inhibits geological analysis, models of crustal thickness variation can inform stretching history and hence validate kinematic models. The average crustal thickness across West Antarctica is ~27 km (e.g., Ritzwoller et al., 2001). Crustal thinning localized beneath deep, narrow rift basins in central West Antarctica has been attributed to focused Neogene extension (e.g., LeMasurier, 2008; Winberry & Anandkrishnan, 2004). Coincident seismic low-velocity anomalies in the uppermost mantle attributed to rift-related thermal perturbation support this hypothesis (e.g., Lloyd et al., 2015). Jordan et al. (2010) invoke a two-stage rifting model whereby pervasive Late Cretaceous rifting (thinning the crust of the

eastern WARS from ~35 to ~26 km) is followed by a Cenozoic phase of narrow-mode rifting causing localized extension in the Amundsen Sea Embayment. Following Jordan et al. (2010), mapped lateral deviations in crustal thickness from ~26 km can serve as a proxy for differential Cenozoic stretching in the eastern WARS. More broadly, mapping the 3-D seismic velocity structure of the crust can help constrain the tectonic provenance and evolution of West Antarctica as a whole.

Seismic anisotropy can further inform structure and deformational history (e.g., Weiss et al., 1999). Structural or compositional layering in the crust can produce seismic anisotropy (e.g., Rabbel & Mooney, 1996), as can the alignment through deformation of intrinsically anisotropic minerals such as mica and amphibole in the crust (e.g., Godfrey et al., 2000; Ko & Jung, 2015; Siegesmund et al., 1989; Tatham et al., 2008; Weiss et al., 1999) and olivine in the upper mantle (e.g., Long & Silver, 2009; Savage, 1999). Radial anisotropy (transverse isotropy with a vertical symmetry axis) in the crust and upper mantle manifests as a difference in the velocities of vertically and horizontally polarized horizontally propagating shear waves ( $V_{SV}$  and  $V_{SH}$ , respectively). Because Rayleigh and Love surface waves predominantly encode  $V_{SV}$  and  $V_{SH}$ , respectively, radial anisotropy is evidenced when an isotropic velocity model ( $V_{SV} = V_{SH}$ ) is unable to simultaneously satisfy Rayleigh and Love wave dispersion data, the so-called Rayleigh-Love discrepancy (e.g., Moschetti et al., 2010). The strength of radial anisotropy, RA, can be quantified as

$$RA = \frac{V_{SH} - V_{SV}}{V_{SV}}, \quad (1)$$

with positive radial anisotropy ( $V_{SH} > V_{SV}$ ) a persistent feature of the Earth's upper mantle (e.g., Shapiro & Ritzwoller, 2002). Radial anisotropy of ~3–6% has been inferred in the uppermost mantle beneath West Antarctica (Ritzwoller et al., 2001).

Positive radial anisotropy in the middle to lower crust in Cenozoic (>5%; Moschetti et al., 2010) and Mesozoic (4–6%; Guo, Yang, et al., 2016) extensional provinces in the western United States and northeast China, respectively, has been attributed to the lattice-preferred orientation of anisotropic minerals by extensional deformation. However, positive radial anisotropy of magnitude ~4–5% is also observed in the middle crust of ancient cratonic and adjacent transitional craton-to-cordillera terranes in northwestern Canada (Dalton & Gaherty, 2013), a setting that stands in marked contrast to tectonically young, extensional provinces. Dalton and Gaherty (2013) attribute the positive middle crustal radial anisotropy in northwestern Canada to metamorphic assemblages in the cratonic crust and a thick, layered metasedimentary package in the adjacent transitional craton-to-cordillera terrane. They suggest that this may indicate the ubiquity of anisotropy in continental crust.

Due to the relative seismic quiescence of the Antarctic continent (e.g., Reading, 2007), long-period surface waves from distant (teleseismic) earthquakes are a mainstay for probing 3-D Antarctic upper mantle structure (e.g., An et al., 2015; Heeszel et al., 2016; Ritzwoller et al., 2001). Shorter-period (typically less than ~25 s) surface waves transiting in the more compositionally heterogeneous crust are subject to more scattering, multipathing and attenuation. The longer the propagation path, the greater the wavefield complexity garnered—especially if paths cross terrane or plate boundaries. This renders teleseismic surface waves at periods less than ~25 s, which are mainly sensitive to crustal structure, difficult to interpret.

Ambient seismic noise refers to the diffuse energy field excited by ocean swells and infragravity waves interacting with the seafloor (e.g., Rhie & Romanowicz, 2004). Its spectral power is highest in the primary (~10–20 s) and secondary (~5–10 s) microseismic bands (e.g., Yang & Ritzwoller, 2008). Cross-correlating the ambient noise field at two locations approximates the impulse response of the Earth between the locations, that is, the Green's function (e.g., Campillo & Paul, 2003; Shapiro et al., 2005). A seismic station can thus serve as a local, virtual earthquake source for other stations. In the case of Antarctica, this circumvents reliance on complex teleseismic surface waves for probing crustal structure. Ambient noise correlation has proved to be a valuable technique in determining the structure of the crust and uppermost mantle in Antarctica (e.g., Pyle et al., 2010; Shen et al., 2018).

In this study, we (i) use 8- to 25-s-period Rayleigh waves extracted from seismic ambient noise to map the 3-D  $V_{SV}$  structure of the West Antarctic crust and uppermost upper mantle. In particular, we aim to constrain the structure and evolution of the eastern WARS via inferred variations in crustal thickness extracted from the  $V_{SV}$  model. To this end, new data from the 2016–2018 UK Antarctic Seismic Network (UKANET; Figure 1)

offer enhanced resolution across a hitherto seismically unsurveyed tract of West Antarctica. We (ii) use the combination of 8- to 25-s-period Rayleigh and Love wave dispersion data along selected interstation paths to make the first estimates of crustal radial anisotropy in West Antarctica, analyzing variations across the mosaic of tectonic blocks comprising West Antarctica and speculating on causative mechanisms.

## 2. Tectonic Setting

East Antarctica coalesced from Archean nuclei in the Mesoproterozoic (1.6–1.0 Ga), ultimately forming the core of the Gondwana supercontinent (e.g., Dalziel, 1992). The emplacement of the Karoo-Ferrar large igneous province in Southern Africa and East Antarctica at ~185–177 Ma preceded the breakup of Gondwana (e.g., Fitzgerald, 2002; Storey & Kyle, 1997, and references therein) and the development of the Weddell Sea Rift System, a broad transtensional province within a distributed plate boundary between East and West Antarctica (e.g., Jordan et al., 2017). Karoo-Ferrar magmatism has been linked to a proposed mantle plume in the proto-Weddell Sea region, potentially an agent of Gondwana breakup (e.g., Elliot & Fleming, 2000; Ferris et al., 2000; Storey & Kyle, 1997).

West Antarctica is considered a mosaic of crustal blocks separated by subglacial depressions (Figure 1). Three of the main four blocks—Marie Byrd Land (MBL), Thurston Island, and the Antarctic Peninsula—are fore-arc and magmatic-arc terranes developed along the paleo-Pacific margin of Gondwana (e.g., Dalziel, 1992). The fourth block, the Haag-Ellsworth Whitmore Mountains (HEW) block, is considered an allochthonous continental fragment translated and rotated from a pre-Gondwana breakup location close to the East Antarctic plate and/or to Southern Africa. Exposed lithologies in the HEW block include a ~13-km-thick stratigraphic succession of Paleozoic metasedimentary and volcanic rocks in the Ellsworth Whitmore Mountains, and Precambrian basement dated to ~1 Ga in the Haag Nunataks (e.g., Curtis, 2001; Jordan et al., 2017; Storey & Kyle, 1997, and references therein).

The West Antarctic tectonic regime switched from transpressional to transtensional following subduction of the Pacific-Phoenix spreading center beneath the paleo-Pacific margin of Gondwana at ~110–105 Ma. The WARS developed as MBL and Thurston Island moved away from the East Antarctic craton. The major extensional phase in the WARS occurred between ~105 and 85 Ma (e.g., Lawver & Gahagan, 1994). Subsequent comparatively modest Paleogene to Neogene extension is recorded in the western Ross Sea (e.g., Cande et al., 2000; Granot & Dymant, 2018). An analogous two-stage model of diffuse Cretaceous rifting in the eastern WARS followed by a Cenozoic phase of narrow rifting causing localized extension in the Amundsen Sea Embayment has been proposed by Jordan et al. (2010).

## 3. Seismic Arrays

The International Polar Year 2007–2008 prompted the first year-round deployment of broadband seismometer arrays in the interior of Antarctica. As part of the Polar Earth Observing Network Antarctic Network (POLENET-ANET) project, a backbone array was deployed across Antarctica (Figure 1). This extant array consists of a mixture of cold-rated Güralp CMG-3T 120 s and Nanometrics Trillium 240 s seismometers sampling at 1 and 40 samples per second (sps).

Denser temporary arrays have intermittently supplemented the POLENET-ANET backbone array in West Antarctica. The most recent of these was the 2016–2018 UKANET array (Brisbourne et al., 2016), comprising 10 cold-rated Güralp CMG-3T 120 s seismometers sampling at 1 and 100 sps (Figure 1 and supporting information Table S1). The UKANET array and 2015–2017 POLENET-ANET mini-array were designed as complementary networks (Figure 1). At the end of the first year of deployment the UKANET array was reconfigured to bolster station coverage along the southern Antarctic Peninsula; this was a pressing concern because of sensor failure at station KIBB and the early loss of station FOSS to unanticipated meltwater pooling (Table S1). Snow accumulation at the UKANET Pine Island Glacier stations was variable, ranging from ~0.25 to ~2.2 m over the 11-month period between initial deployment and servicing. These are reported in Johnson et al. (2018) and may help inform logistical considerations for the International Thwaites Glacier Collaboration.

The Antarctic Seismographic Argentinean Italian Network (ASAIN), station PMSA of the Global Seismographic Network (GSN), and the 1997–1999 Seismic Experiment in Patagonia and Antarctica network (SEPA) provide additional coverage (Figure 1).

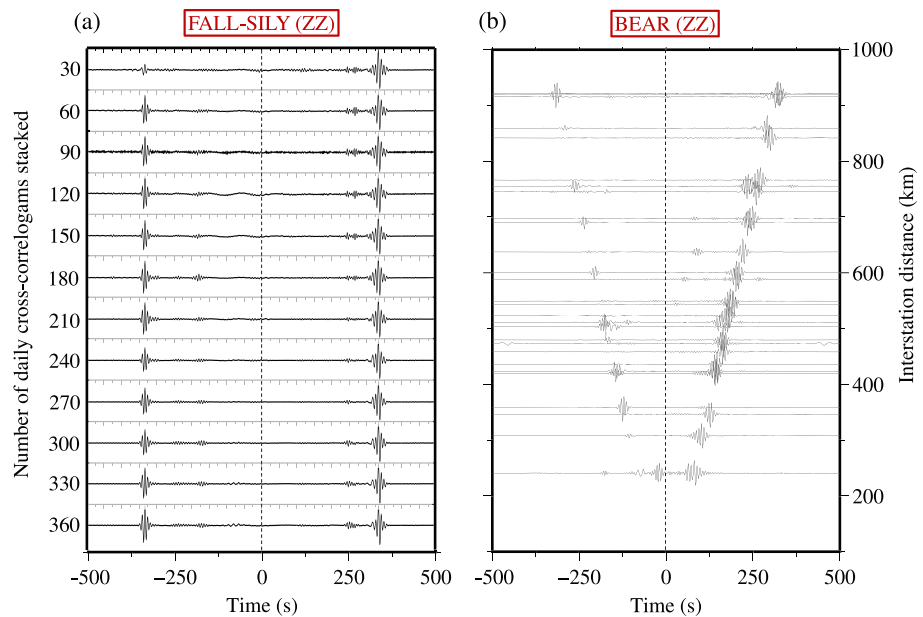


**Figure 2.** (a) Stacked causal (positive correlation time lags) and acausal (negative correlation time lags) vertical-component cross correlograms for POLENET station pair FALL-SILY as a function of the number of daily cross correlograms contributing to the stack. Stacking as little as 1 month of daily cross correlograms in Antarctica is sufficient to yield high signal-to-noise ratio seismograms. For UKANET-UKANET and UKANET-POLENET station pairs, a minimum of 1 year of contemporaneous data was typically available, but for POLENET-POLENET station pairs several years of contemporaneous data were generally available. (b) Stacked causal and acausal vertical-component cross-correlogram record section ordered by interstation distance centered at POLENET station BEAR on the Marie Byrd Land coast (see Figure 1 for station locations). The asymmetry in the causal and acausal cross correlograms is typical of coastal stations: the comparatively higher amplitude causal signals reflect the predominance of seismic noise incident from the adjacent coast; the comparatively low-amplitude acausal signals reflect noise incident from the continental interior.

#### 4. Data Processing and Phase Velocity Measurement

For stations of the UKANET, POLENET, ASAIN, SEPA, and GSN networks shown in Figure 1, we calculated vertical- and horizontal-component cross correlations for all contemporaneous stations over the time periods 1997–1999 and 2008–2018. As an initial step, instrument responses, means, and trends were removed from the 1-sps vertical- (Z) and horizontal-component (E, N) seismograms and these were subsequently filtered between 4 and 80 s using a zero-phase-shift Butterworth filter. Cross correlograms were then calculated from hour-long seismograms for all station pairs for components ZZ, EE, EN, NE, and NN using the phase-based coherence functional of Schimmel (1999). For UKANET-UKANET and UKANET-POLENET station pairs, a minimum of 1 year of contemporaneous data was typically available, but for POLENET-POLENET station pairs several years of contemporaneous data were generally available. The resultant cross correlograms were stacked in order to boost the signal-to-noise ratio using the time-frequency domain phase-weighted stacking algorithm developed by Schimmel and Gallart (2007) and Schimmel et al. (2011; Figure 2a). As noted by others (e.g., Pilia et al., 2016; Ren et al., 2013), we found that the phase-based coherence functional and time-frequency domain phase-weighted stacking better suppress incoherent noise than traditional amplitude-based coherence and stacking techniques (Figure S1a).

Asymmetry between causal (positive correlation time lags) and acausal (negative correlation time lags) portions of the cross correlograms related to noise directivity is common in ambient noise studies (e.g., Yang & Ritzwoller, 2008). In Antarctica, the asymmetry is most pronounced when one station is located close to the coast and the other in the continental interior. In this case, the comparatively higher amplitude signal reflects seismic noise incident from the adjacent coast, while the lower amplitude signal reflects (attenuated) noise incident from the continental interior (Figure 2b). Although dominant noise sources are generally distributed inhomogeneously in azimuth, Yang and Ritzwoller (2008) demonstrate that sufficiently strong ambient noise (signal-to-noise ratio > 10) emerges from most azimuths over the course of a year to guarantee reliable retrieval of empirical Green's functions.

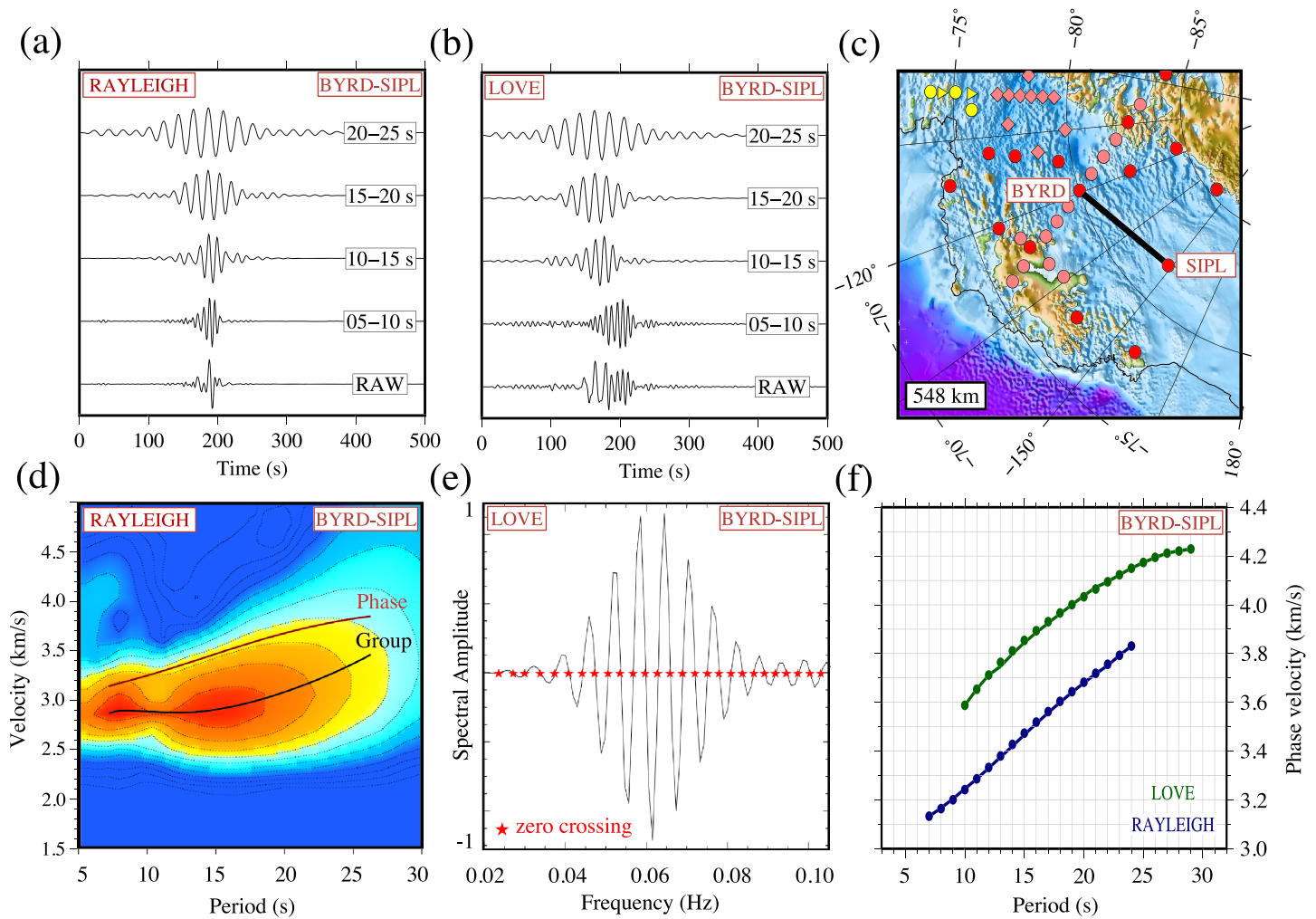


**Figure 3.** (a) Stacked vertical- and (b) transverse-component symmetric cross correlograms for POLENET station pair BYRD-SIPL filtered in several period bands. Rayleigh and Love waves are the dominant phases, respectively. In this case of BYRD-SIPL, 7 years of daylong seismograms contributed to the stacked symmetric cross correlograms shown. (c) Map of station locations. (d) Automated frequency-time analysis-inferred Rayleigh wave group and phase velocities for interstation path BYRD-SIPL. (e) The real spectrum of the BYRD-SIPL transverse-component symmetric cross correlogram with zero crossings marked. (f) Rayleigh and Love wave phase velocity dispersion for interstation path BYRD-SIPL inferred by AFTAN (continuous lines) and the spectral method (dots).

Following stacking, the causal and acausal parts of the resultant cross correlograms were averaged to give the “symmetric” cross correlograms. Radial- and transverse-component symmetric cross correlograms were finally derived by applying the rotation operator described in Lin et al. (2008) to the various horizontal-component symmetric cross-correlogram pairs (Figure S1b). The vertical- and radial-component cross correlograms both encode interstation Rayleigh wave dispersion information, but the vertical-component generally has a higher signal-to-noise ratio (e.g., Lin et al., 2008); the transverse-component cross correlograms encode interstation Love wave dispersion information. Like Lin et al. (2008), we therefore based our Rayleigh and Love wave dispersion analysis on the vertical- and transverse-component cross correlograms, respectively.

Through the application of multiple narrow-band filters, cross-correlogram signal power as a function of frequency (or period) can be inferred (“frequency-time analysis”; e.g., Dziewonski et al., 1969). To be considered for analysis here, cross correlograms had to have a signal-to-noise ratio greater than 10 and the interstation distance had to be at least two wavelengths for a given period (e.g., Lin et al., 2009). We used automated frequency-time analysis (AFTAN; e.g., Bensen et al., 2007; Levshin & Ritzwoller, 2001; Lin et al., 2008) to extract fundamental mode Rayleigh and Love wave interstation phase velocities from the cross correlograms in the period range 8–25 s where the spectral power is high (Figure 3). Pilot Rayleigh and Love wave phase velocity dispersion curves were employed to mitigate the  $2n\pi$  cycle ambiguity inherent in phase

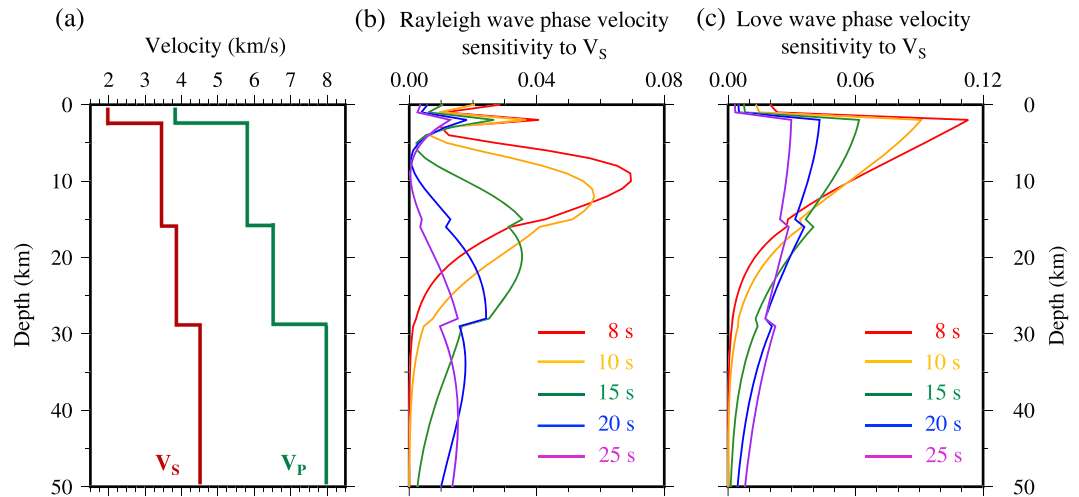


**Figure 4.** (a) Representative 1-D shear ( $V_S$ ) and compressional ( $V_P$ ) velocity models for West Antarctica used to mitigate the  $2n\pi$  cycle ambiguity inherent in phase velocity determination. Sensitivity kernels of fundamental mode (b) Rayleigh and (c) Love wave phase velocities to  $V_S$  at periods 8, 10, 15, 20, and 25 s calculated for the structure shown in (a). The phase velocity sensitivity kernels peak deeper and are heavier tailed as the period increases.

velocity determination (e.g., Bensen et al., 2007; Ekström et al., 2009; Lin et al., 2008). The pilot curves were calculated for a representative 1-D West Antarctic velocity model comprising a 2-km-thick ice sheet atop 27-km-thick crust (e.g., Ritzwoller et al., 2001) with crustal velocities from AK135 (Kennett et al., 1995) and upper mantle half-space velocities from the regional waveform modeling study of O'Donnell et al. (2017; Figure 4a).

In the frequency domain, the ambient noise cross correlogram approximates a Bessel function of the first kind and phase velocities at discrete frequencies can be extracted by associating zeros of the observed spectra with corresponding zeros of the Bessel function (e.g., Ekström et al., 2009; Figure 3e). We compared the AFTAN-inferred phase velocities with those derived from the zero crossings of the real cross-correlogram spectra and found both measurements to be consistent within  $\sim 0.01$  km/s (Figure 3f). Figure S1c meanwhile compares AFTAN-inferred Rayleigh wave phase velocities from phase- and amplitude-based coherence functionals, showing them to be consistent to within  $\sim 0.01$  km/s. We therefore adopted 0.02 km/s as a representative phase velocity uncertainty estimate.

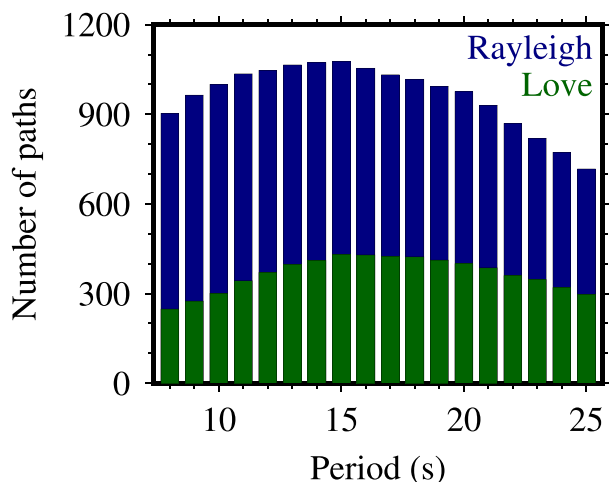


**Figure 5.** Number of interstation paths yielding viable Rayleigh (blue) and Love (green) wave phase velocity measurements as a function of period.

The uncertainty of phase velocity measurements is smaller than that of group velocity measurements, and at a given period, phase velocities are sensitive to deeper structure than group velocities (e.g., Lin et al., 2008). Here our focus is on the middle to lower crust beneath West Antarctica, and phase velocities are therefore our target. In a companion study the ambient noise-inferred 8- to 25-s Rayleigh wave phase velocity dispersion data are merged with longer-period (20–143 s) Rayleigh wave phase velocity dispersion data extracted from two-plane wave analysis of earthquake data to better model the upper mantle structure of West Antarctica (O'Donnell et al., 2019). Figures 4b and 4c show the depth sensitivity of fundamental mode Rayleigh and Love wave phase velocities to shear wave velocity for the representative West Antarctic velocity model of Figure 4a. In the period range 8–25 s, the phase velocity data constrain crustal and uppermost upper mantle structure.

The transverse-component cross correlograms generally exhibited a lower signal-to-noise ratio than vertical-component counterparts. We speculate that this is rooted in tilting of the seismometers by local settling of the snow pack. For this reason we were able to extract comparatively fewer interstation Love wave phase velocity measurements. Out of a total of 2,041 unique interstation paths, 1,196 paths yielded viable Rayleigh

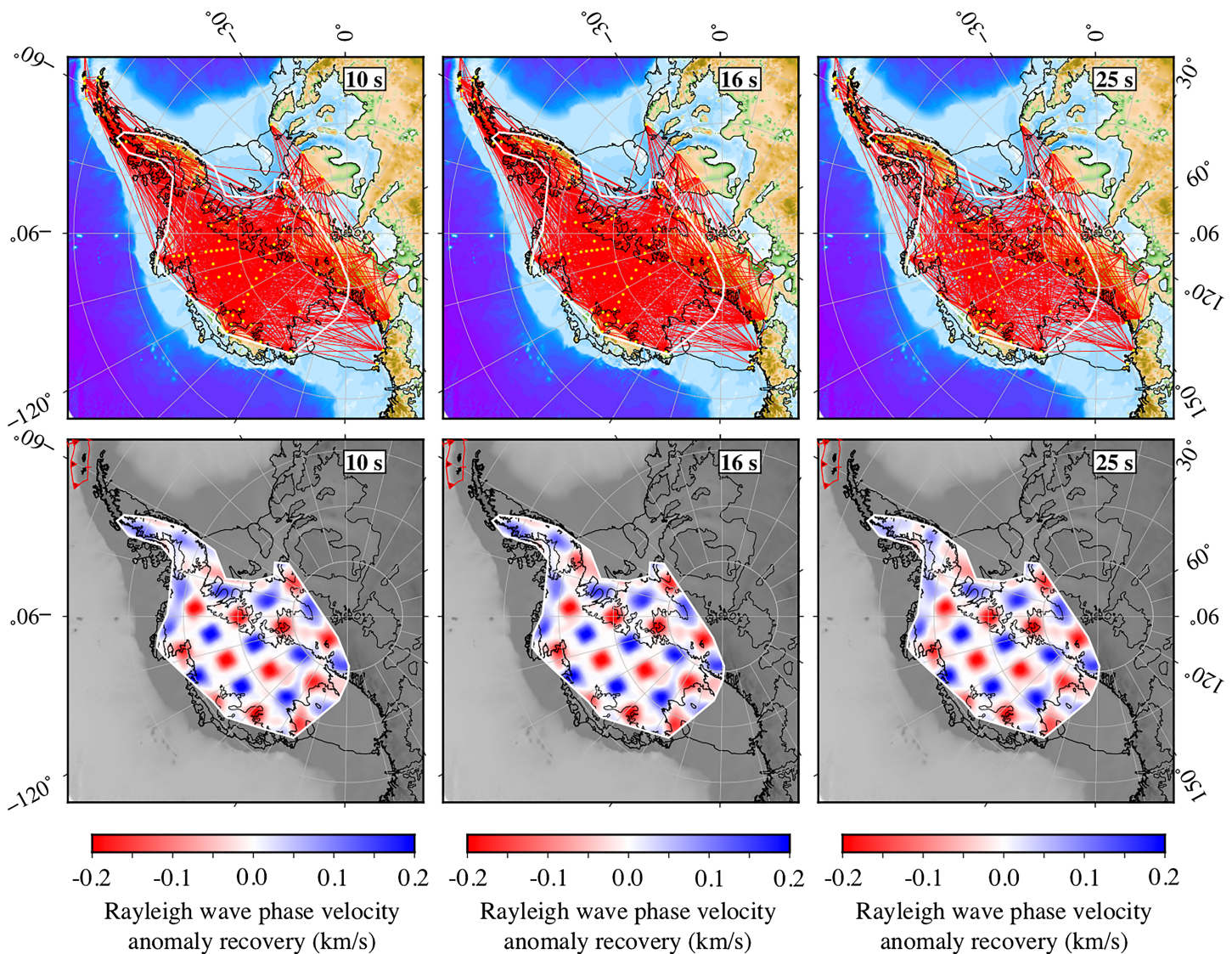


**Figure 6.** (Top) Interstation paths constraining the Rayleigh wave ambient noise tomography at periods 10, 16, and 25 s. Tomographic resolution depends on the density of interstation paths and their crossing. Yellow dots are station locations. The BEDMAP2 bedrock 2,000-m elevation contour approximately delineates the HEW block and MBL topographic dome. (Bottom) Tomographic resolution is assessed by recovery tests of synthetic checkerboard patterns of velocity anomalies of magnitude  $\pm 0.2$  km/s and wavelength 300 km. The white polygon delineates the region of credible resolution. MBL = Marie Byrd Land; HEW = Haag-Ellsworth Whitmore Mountains.

wave phase velocity dispersion curves and 560 paths yielded viable Love wave phase velocity dispersion curves. Figure 5 shows a histogram of the number of interstation paths yielding viable Rayleigh and Love wave phase velocity measurements as a function of period in the range 8–25 s.

### 5. Phase Velocity Tomography

We used the Fast Marching Surface Tomography (FMST) package developed by Rawlinson and Sambridge (2005) to create 2-D phase velocity maps at periods 8–25 s from the ensemble of interstation phase velocity measurements. At each period, the ensemble mean interstation phase velocity was used as a starting velocity. In FMST, velocities are defined by a grid of nodes with bicubic B-spline interpolation and the forward problem of traveltimes prediction uses the fast marching method, a grid-based eikonal-solver (Rawlinson & Sambridge, 2004; Sethian & Popovici, 1999). The method implements a gradient-based subspace inversion scheme (Kennett et al., 1988) in which velocities are adjusted to optimize the match between observed and predicted traveltimes, subject to damping and smoothing regularization. For the tomography we used a grid



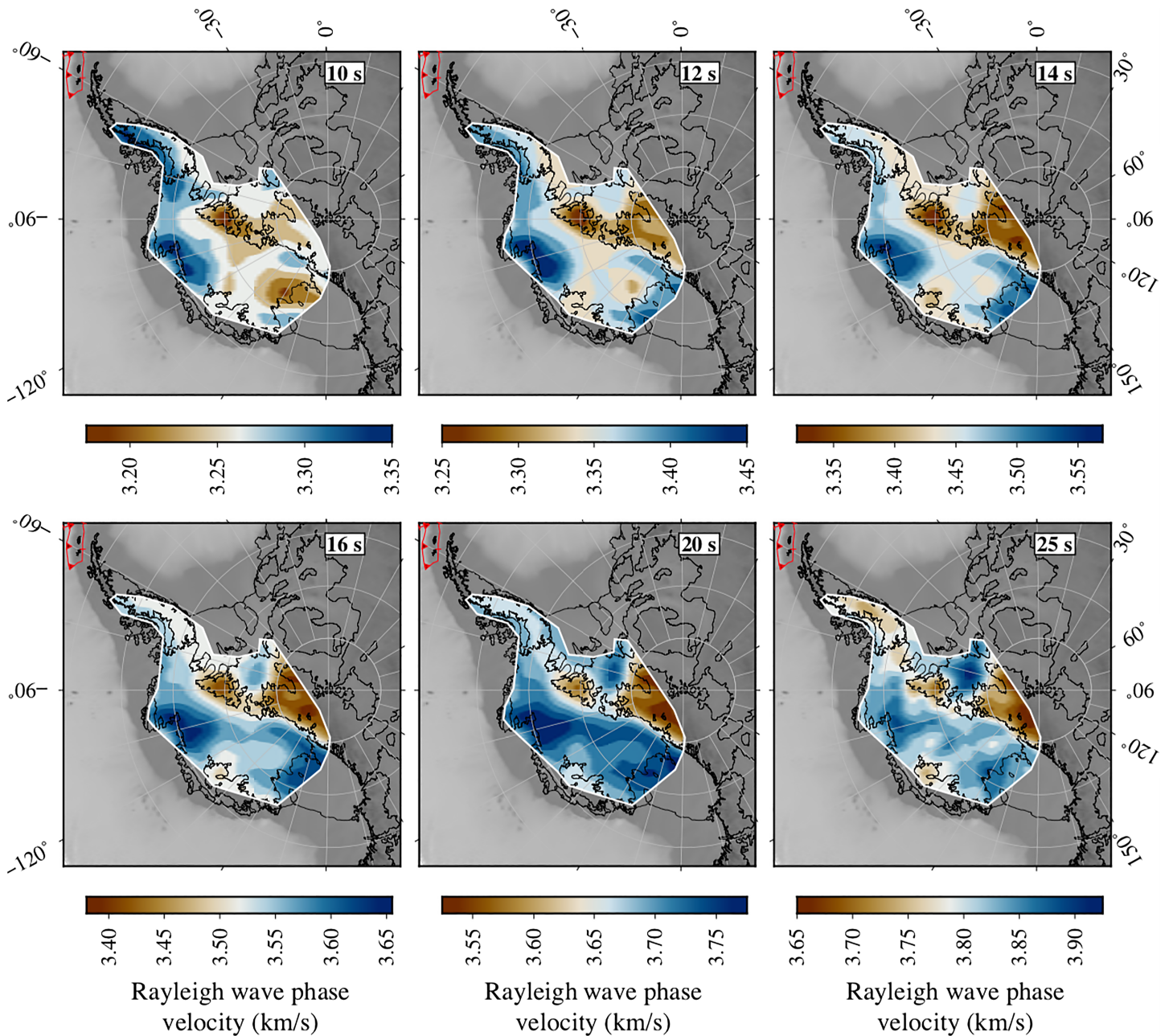


**Figure 7.** Rayleigh wave phase velocity maps at a selection of periods.

with a node spacing of  $0.75^\circ$ . Because FMST uses geographic coordinates, we translated our stations and grid to equatorial latitudes to perform the inversions in order to circumvent the geographic grid distortion that occurs at high latitudes. Following inversion, the inverse coordinate translation was applied to the inferred 2-D phase velocity maps.

Tomographic resolution depends on crossing paths. Figure 6 (top) shows the interstation paths constraining the Rayleigh wave phase velocity tomography at periods 10, 16, and 25 s. The sparser ensemble of interstation Love wave phase velocity measurements (see Figure 5) did not offer comparable resolution so we did not pursue Love wave tomography; instead, we analyzed Love wave phase velocities along selected interstation paths, as discussed in section 8. The resolving capability of the Rayleigh wave tomography was quantified by means of checkerboard recovery tests (Figure 6, bottom). For each period, interstation Rayleigh wave travel times were calculated through a synthetic pattern of alternating velocity anomalies of magnitude  $\pm 0.2$  km/s

and wavelength 300 km. Using the same interstation path geometry as the actual data inversion, the travel times were then inverted from a uniform starting model in a bid to recover the initial checkerboard structure. The morphology and amplitude of velocity anomalies of wavelength 300 km is recovered with high fidelity in central West Antarctica. Resolution degrades on the Antarctic Peninsula as the interstation path crossing decreases. In this region anomaly morphologies are smeared and amplitude recovery is no better than ~50%. We confine subsequent discussion of imaged structure to the region enclosed by the polygon in Figure 6. Appropriate smoothing and damping values for the tomography were selected based on trade-off analyses carried out systematically at each period (Figure S2).

Both systematic and random errors contribute to phase velocity uncertainty, with systematic biases (e.g., arising from a particular regularization choice) more difficult to reliably estimate. To estimate the phase velocity uncertainty at a given period due to systematic error, we repeated the tomography for a suite of smoothing and damping combinations in the vicinity of the “knee” of the regularization trade-off curves (Figure S2). The resultant mean deviation in phase velocities between these models and our preferred model (smoothing 25, damping 0.1) is generally less than ~ 0.03 km/s at all periods. The FMST code does not output a covariance matrix, so we estimated the phase velocity uncertainties due to random errors from the root-mean-square (RMS) travel time residuals through the inferred 2-D phase velocity maps. The RMS residuals were generally less than 2.5 s (Figure S3), which translates to a phase velocity uncertainty of <~0.01 km/s. These estimations of systematic and random errors combine to give upper bound Rayleigh wave phase velocity uncertainties of ~ 0.05 km/s at all periods.

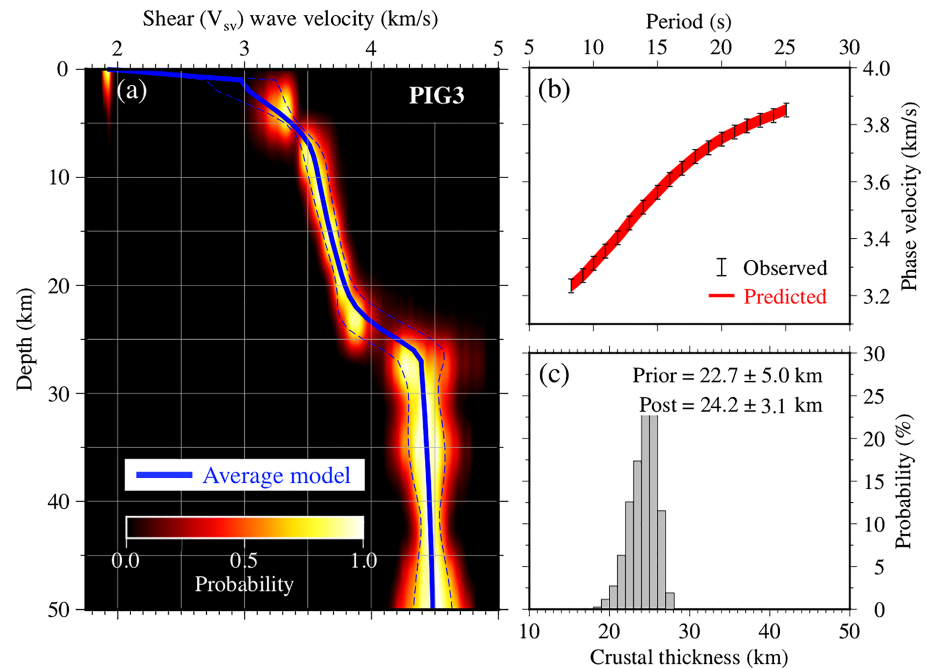
## 6. Rayleigh Wave Phase Velocity Maps

Figure 7 shows resulting Rayleigh wave phase velocity maps at a selection of periods. At the longer periods shown (e.g., 16–25 s), Rayleigh waves are highly sensitive to the large impedance contrast of the crust-mantle transition: Lower velocities generally delineate where the Rayleigh waves are predominantly sampling crustal rock, whereas higher velocities are generally indicative of comparatively thinner crust through the increased influence of seismically faster mantle rock. The geographical coincidence of lower phase velocities with elevated topography is striking but not unexpected given the model of Airy isostasy. The higher phase velocities characterizing the WARS contrast starkly. As a proxy for crustal thickness, the amplitudes and geographic distribution of velocity anomalies at these periods is broadly consistent with results from receiver function (e.g., Chaput et al., 2014; Ramirez et al., 2016, 2017), surface wave (e.g., An et al., 2015; Shen et al., 2018), and gravity (e.g., Damiani et al., 2014; Jordan et al., 2010; O'Donnell & Nyblade, 2014; Pappa et al., 2019) studies.

## 7. Shear Wave ( $V_{SV}$ ) Velocity Model

The sensitivity kernels of fundamental model Rayleigh wave phase velocities to shear wave structure (e.g., Figure 4b) enable the development of 3-D  $V_{SV}$  models from 2-D phase velocity maps. We performed two suites of inversion for shear wave velocity structure: (i) inversion for 1-D  $V_{SV}$  structure at each 0.75° grid node using local Rayleigh wave dispersion curves extracted from the 2-D phase velocity maps by sampling at each second from 8–25 s and (ii) inversion for 1-D interstation average  $V_{SV}$  and  $V_{SH}$  structure for those interstation paths for which high-quality Rayleigh and Love wave dispersion data were available. The first suite of inversions was used to build a 3-D  $V_{SV}$  model of the West Antarctic crust, the second suite to probe the depth, strength, and spatial variation of crustal radial anisotropy across the mosaic of tectonic blocks comprising West Antarctica. We defer discussion of the anisotropic inversion and results until section 8, focusing firstly on the construction and interpretation of the 3-D  $V_{SV}$  model.

For this inversion the  $V_{SV}$  models were parameterized by ice and/or water layers overlying crustal and uppermost mantle layers, the latter two described by cubic splines. Ice thicknesses and water depths were taken from BEDMAP2 (Fretwell et al., 2013) and allowed to vary within their published uncertainty limits. The ice shear wave velocity was permitted to range between 1.82 and 2.02 km/s with a density fixed at 910 kg/m<sup>3</sup>. The sub-ice/water  $V_{SV}$  crustal layer was parameterized using four cubic B-splines and a crustal thickness permitted to vary ±5 km from initial estimates extracted from the An et al. (2015) Antarctic crustal model. The  $V_{SV}$  uppermost mantle layer was parameterized using five cubic B-splines to a depth of 70 km, below which Preliminary Reference Earth Model (Dziewonski & Anderson, 1981)  $V_{SV}$  values were adopted. We imposed the constraint that velocities must increase at the crust-mantle transition (i.e., uppermost man-



**Figure 8.** (a) Vertically polarized shear wave velocity ( $V_{SV}$ ) profile at UKANET station PIG3 inferred from (b) corresponding Rayleigh wave phase velocity dispersion curve. The thick blue line is the mean  $V_{SV}$  velocity, the blue dashed lines are one standard deviation bounds. Zero-kilometer depth corresponds to the local elevation of the ice sheet surface at PIG3. The ice thicknesses and velocities are relatively well known from independent surveys (e.g., Fretwell et al., 2013) and thus function as de facto constraints in the  $V_{SV}$  inversions. (c) The prior and posterior crustal thickness estimates at PIG3.

tle velocities exceed lower crustal velocities). Compressional wave velocities and densities were scaled from shear wave velocities using regressions reported in Brocher (2005). Although the ice/water layer thicknesses and velocities are technically model parameters, they are well known (e.g., Fretwell et al., 2013) and function as de facto constraints. Ten model parameters thus describe the underlying crustal and uppermost mantle structure: four crustal cubic B-spline coefficients, the crustal thickness, and five mantle cubic B-spline coefficients.

In a Bayesian framework, we permitted crustal and uppermost mantle shear wave velocities to explore a broad  $\pm 20\%$  range around initial PREM  $V_{SV}$  velocities, with layer thicknesses free to explore the aforementioned ranges. This suite of constraints informed the prior model probability density function (PDF). The likelihood function for dispersion curve prediction used the *Mineos* package (Masters et al., 2011). A Markov chain Monte Carlo sampling scheme based on the Delayed Rejection Adaptive Metropolis algorithm (DRAM; Haario et al., 2006) built the posterior model PDF (Guo, Chen, et al., 2016; Guo, Yang, et al., 2016; Shan et al., 2014, and references therein). In an initial nonadaptive stage, 60,000 samples were drawn from the prior PDF and used to construct a proposal distribution. In an ensuing adaptive stage, the proposal distribution was updated every 10,000 samples a total of 10 times. The statistics of the posterior PDF were calculated from the final 2,500 accepted samples in the chain.

An example of the 1-D  $V_{SV}$  inversion is shown for UKANET station PIG3 in Figure 8. The standard deviation of inferred  $V_{SV}$  velocities at PIG3 is generally less than  $\sim 0.1$  km/s in the middle to lower crust, increasing to  $\sim 0.25$  km/s around the crust-mantle transition, and representative of the suite of 1-D  $V_{SV}$  profiles. At PIG3,  $V_{SV}$  velocities increase gradually from  $\sim 3.5$  km at  $\sim 7$  km depth to  $\sim 3.8$  km at  $\sim 22$  km depth. This is a velocity range that encompasses anticipated common middle and lower crustal rock types (e.g., Holbrook et al., 1992). The sub-ice shallow crustal  $V_{SV}$  structure is not well constrained by our shortest period (8 s) Rayleigh wave data and not interpreted. The transition from crustal lithologies to ultramafic mantle rock at the Moho is characterized by an increase in shear velocities to values exceeding  $\sim 4.3$  km/s (e.g., Ramirez et al., 2017, and references therein) and occurs at  $\sim 24 \pm 3$  km depth beneath PIG3 (Figure 8). However, because surface waves are insensitive to abrupt impedance contrasts, we cannot discern whether a sharp crust-mantle transition is masquerading as a gradual transition, and our crustal thickness estimates are in

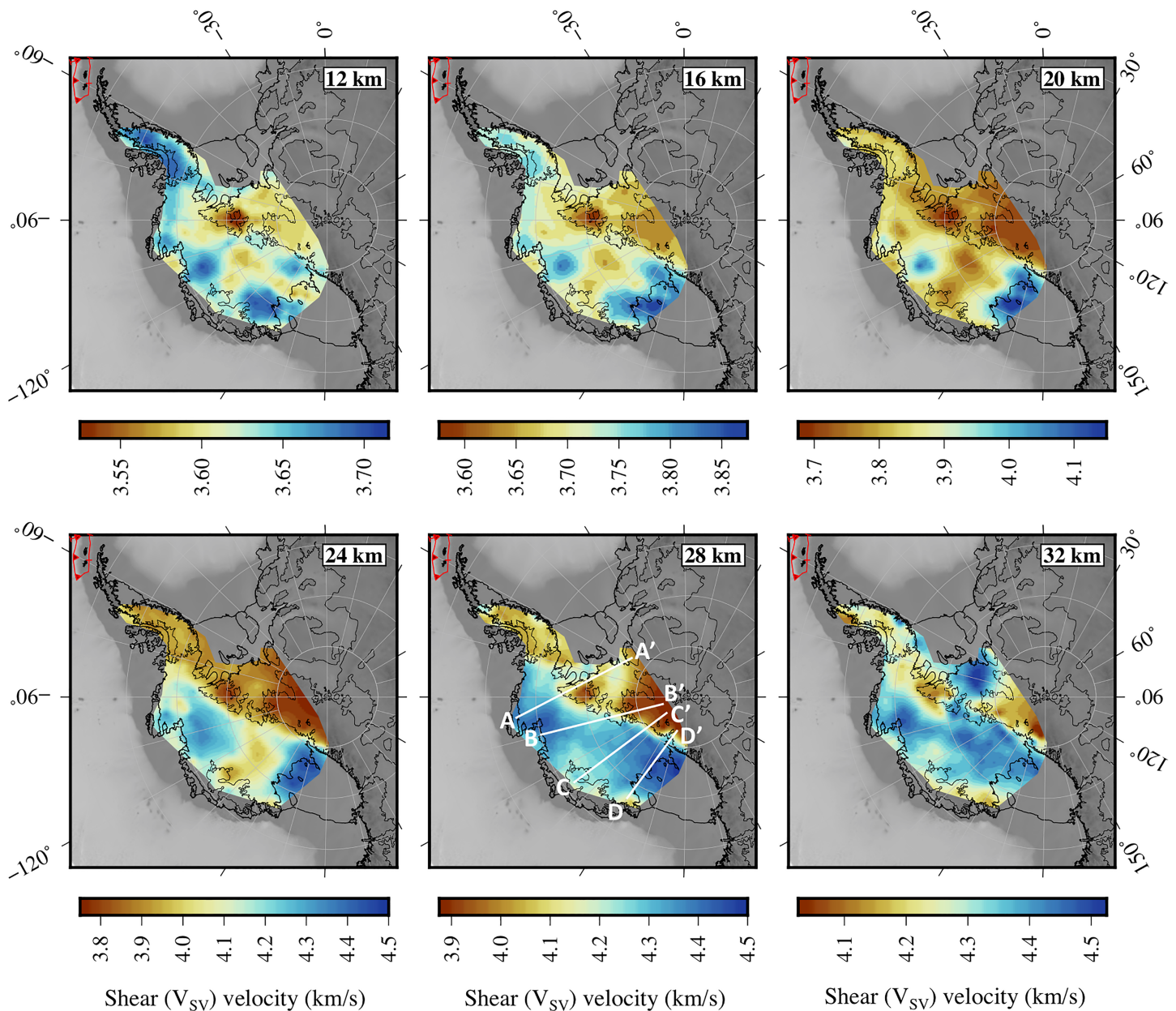


**Figure 9.** Shear wave velocity ( $V_{SV}$ ) maps at a selection of depths. The locations of the vertical  $V_{SV}$  cross sections shown in Figure 10 are superimposed on the 28km depth map.

general subject to an uncertainty of  $\pm \sim 4$  km. That said, the inferred crustal thickness of  $\sim 24$  km at PIG3 is consistent with gravity-based estimates of  $\sim 21$ – $27$  km for the Hudson Mountains north of Pine Island Glacier (Jordan et al., 2010) and compares with an estimated average crustal thickness of  $\sim 27$  km for West Antarctica (Ritzwoller et al., 2001). The uppermost mantle  $V_{SV}$  at PIG3 ranges from  $\sim 4.4$ – $4.5$  km/s with an attendant standard deviation of  $\sim 0.2$  km/s.

### 7.1. Tectonic Interpretation of $V_{SV}$ Model

While the insensitivity of surface waves to sharp impedance contrasts renders them a less accurate estimator of crustal thickness than, for example, receiver function spot measurements, considerable tectonic insight can be gleaned from the lateral velocity variations mapped by surface waves. Figure 9 shows 2-D  $V_{SV}$  maps at a selection of depths constructed by gridding the suite of 1-D  $V_{SV}$  profiles, and Figure 10 shows vertical  $V_{SV}$  cross sections along four profiles spanning the WARS. The corresponding  $V_{SV}$  standard deviations are shown in Figures S4 and S5. Figure 11 in turn shows a map of crustal thickness determined from the initial

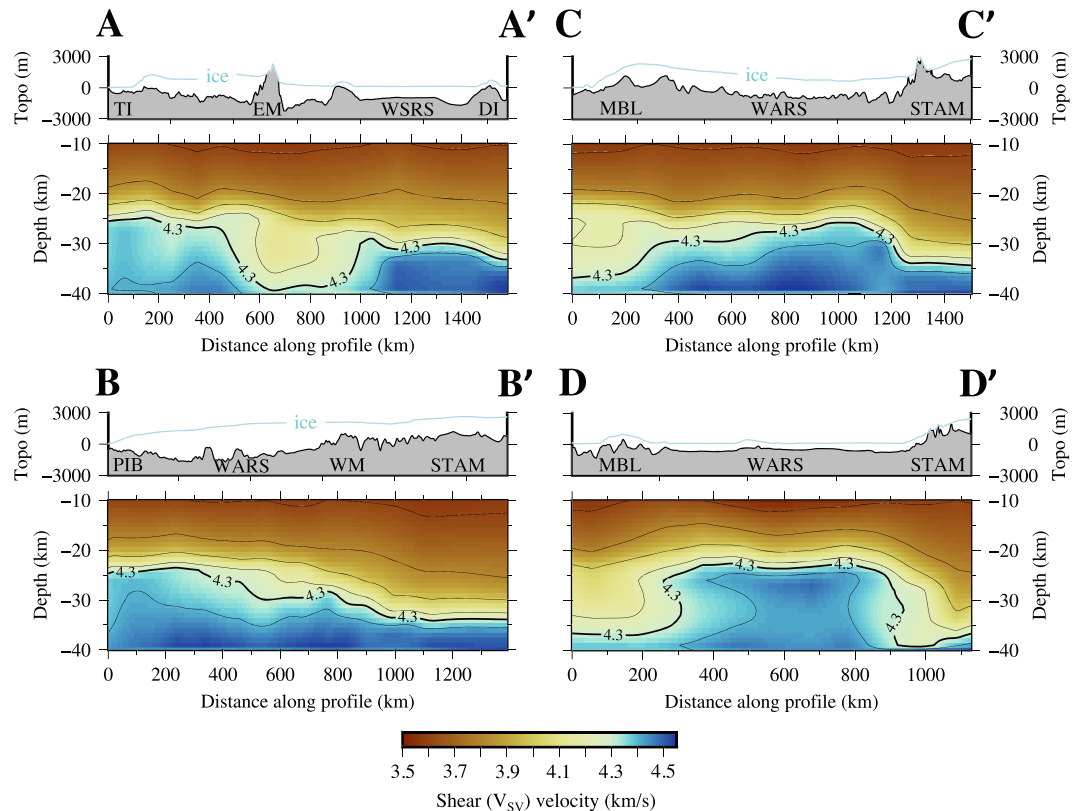


**Figure 10.** Vertical cross sections showing middle to lower crustal and uppermost mantle shear wave velocity ( $V_{SV}$ ) structure along the four profiles spanning the West Antarctic Rift System (WARS) located in Figure 9. The  $V_{SV}$  velocities are contoured at 0.2 km/s intervals, with the 4.3 km/s contour that we take as indicative of the Moho labeled. Corresponding BEDMAP2 ice and bedrock topography (Topo) profiles are shown in each case. EM, Ellsworth Mountains; DI, Dufek Intrusion; MBL, Marie Byrd Land; PIB, Pine Island Bay; STAM, southern Transantarctic Mountains; TI, Thurston Island; WM, Whitmore Mountains; WSRS, Weddell Sea Rift System.

instance in depth of  $V_{SV} > 4.3$  km/s (e.g., Ramirez et al., 2017, and references therein). As described for the 1-D  $V_{SV}$  profile at station PIG3 (Figure 8), Figures S4 and S5 show that  $V_{SV}$  standard deviations are typically less than  $\sim 0.1$  km/s in the middle to lower crust. As anticipated, increased  $V_{SV}$  standard deviations of  $\sim 0.25$  km/s track the crust-mantle transition, before decreasing to less than  $\sim 0.2$  km/s in the uppermost mantle. Thus, our crustal thickness estimates are subject to a typical uncertainty of  $\pm \sim 4$  km.

Figures 9 to 11 suggest that the thinnest WARS crust ( $\sim 22$  km thick) in the modeled region occurs beneath the Ross Ice Shelf and in the vicinity of the Byrd Subglacial Basin (BSB) in the Amundsen Sea Embayment, a pattern consistent with preceding studies. For example, marine seismic refraction and gravity surveys suggest that the crustal thickness of the Ross Sea sector of the WARS ranges  $\sim 17$ – $24$  km (e.g., Siddoway, 2008, and references therein), while localized crustal thinning to 18–20 km beneath the BSB has been inferred from aerogravity data (Damiani et al., 2014; Jordan et al., 2010). In the Bentley Subglacial Trench, receiver function data support crustal thinning to 21 km (Winberry & Anandakrishnan, 2004). Our resolution analysis suggests that structure of wavelength  $\sim 300$  km is recovered with high fidelity in central West Antarctica (see Figure 6). If crustal thinning is localized in rifts narrower than this, we resolve a smeared representation of the actual thinning. Hence our minimum crustal thicknesses generally exceed those modeled by higher-resolution receiver function and aerogravity data.

A ridge of crust  $\sim 26$ – $30$  km thick extending south from the MBL dome separates the domains of highly extended crust in the Ross and Amundsen Sea Embayments (Figure 11). Chaput et al. (2014) and Shen et al. (2018) imaged the same feature. If distributed Cretaceous rifting thinned the WARS crust from  $\sim 35$  to  $\sim 26$  km (e.g., Jordan et al., 2010), this ridge of thicker crust suggests that Cenozoic rifting was not uniform across the WARS, assuming that crustal thickness was similar everywhere in the WARS prior to rifting. Instead, our  $V_{SV}$  model suggests that Cenozoic rifting was concentrated in the Ross Sea and Amundsen

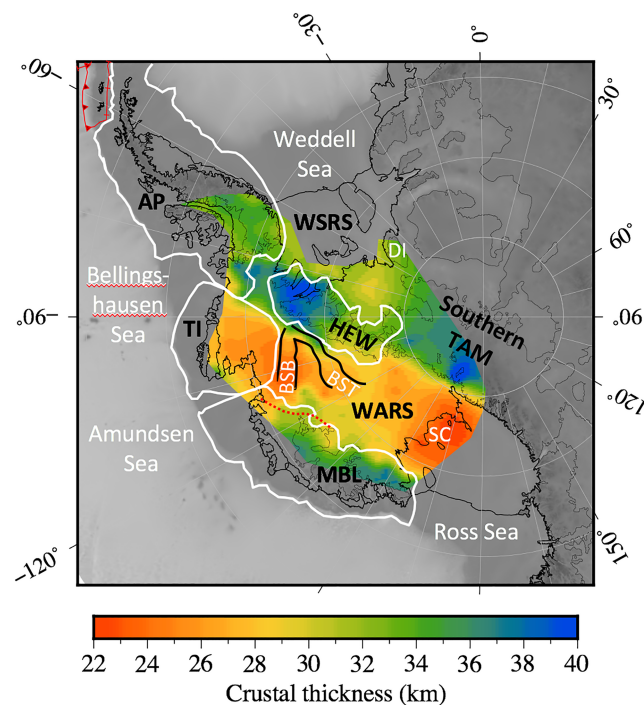


**Figure 11.** Map of crustal thickness (ice layer excluded) based on  $V_{SV}$  model, where the initial instance in depth of  $V_{SV} > 4.3$  km/s is taken as indicative of the Moho. Moho depths are translated to crustal thicknesses using BEDMAP2 bedrock topography and ice thickness data. Following Dalziel and Elliot (1982), white lines delineate major crustal blocks of West Antarctica (AP, Antarctic Peninsula; TI, Thurston Island; MBL, Marie Byrd Land; HEW, Haag-Ellsworth Whitmore Mountains block). Other abbreviated features: BSB, Byrd Subglacial Basin; BST, Bentley Subglacial Trench; DI, Dufek Intrusion; SC, Siple Coast; TAM, Transantarctic Mountains; WARS, West Antarctic Rift System; WSRs, Weddell Sea Rift System. The red dashed line shows the revision to the boundary between the MBL block and WARS suggested by Damiani et al. (2014).

Sea Embayments, which in turn implies along-strike variability in the Cenozoic evolution of the WARS. Recent seismic and magnetotelluric studies similarly point to along-strike variability in the tectonic history of the Transantarctic Mountains (TAM; e.g., O'Donnell et al., 2019; Wannamaker et al., 2017, and references therein).

The southern margin of the WARS is well defined along the southern TAM and HEW block by a sharp seismic velocity and crustal thickness gradient (Figures 9 to 11). The maps suggest that the southern WARS margin continues striking toward the Bellingshausen Sea, coincident with the common boundary of the HEW, Thurston Island, and Antarctic Peninsula crustal blocks (Figure 11). Figure S6 compares our crustal thickness model with that of Shen et al. (2018) in the area of overlap. While the broadscale patterns and thicknesses are generally consistent within mutual uncertainty limits, several differences are apparent. For instance, the Shen et al. (2018) model does not obviously suggest that the southern WARS margin follows the common boundary of the HEW, Thurston Island and Antarctic Peninsula crustal blocks. It instead favors relatively thicker crust within the Thurston Island block, hence reducing/eliminating a crustal thickness gradient at the aforementioned common boundary (Figure S6). The UKANET seismic data bolster resolution in the Thurston Island block (Figure 1) and suggest crustal thicknesses consistent with gravity-based estimates of  $\sim 21$ – $27$  km for the Hudson Mountains north of Pine Island Glacier (Jordan et al., 2010). Jordan et al. (2013) comment on the absence of a connection between the inland extent of the Weddell Sea Rift System and the WARS from aerogeophysical data. We similarly note a lack of any apparent connection between the rift systems in our  $V_{SV}$  model. Loss of resolution toward the coast precludes imaging of any signatures of WARS continuation offshore into the Amundsen or Bellingshausen Seas.

Figure 11 suggests that the thickest crust ( $\sim 35$ – $40$  km) in the modeled region is found beneath the southern TAM and Haag Nunataks-Ellsworth Mountains, with slightly thinner crust occurring beneath MBL and the Antarctic Peninsula. However, the tomographic resolution degrades on the Peninsula (Figure 6), so our modeled crustal thickness there ( $\sim 32$ – $35$  km) is likely underestimated; satellite gravity data suggest that

the crust on the southern Peninsula is comparably thick to that beneath the Ellsworth Mountains (e.g., O'Donnell & Nyblade, 2014; Pappa et al., 2019).

In MBL, the general pattern is of crustal thickness increasing northward from ~28–30 at the southern margin of the block to ~35–38 km in the block interior. The lower crustal  $V_{SV}$  velocities >4.0 km/s beneath MBL (Figure 10) may reflect subduction or rift-related mafic intrusion, potentially in the presence of a mantle plume (e.g., Finn et al., 2005; LeMasurier & Landis, 1996; Siddoway, 2008; Wysoczanski et al., 1995). The significantly thinner crust (~26 km thick) underlying the eastern end of the MBL block within the Amundsen Sea Embayment stands in stark contrast with the rest of the block (Figure 11). Based on analysis of airborne gravity data, Damiani et al. (2014) suggest a revision to the boundary between the MBL block and WARS originally devised by Dalziel and Elliot (1982). Using their revised boundary, much of the region of significantly thinner crust is instead designated part of the WARS (see Figure 11).

We model crust ~35–40 km thick beneath the Haag Nunataks and northern Ellsworth Mountains decreasing to a thickness of ~30–32 km beneath the Whitmore Mountains (Figures 10 and 11). These thickness estimates and their spatial variation are consistent with aerogravity and receiver function studies (e.g., Chaput et al., 2014; Jordan et al., 2010; Ramirez et al., 2017) and the recognition of distinct structural domains within the composite HEW block (e.g., Jordan et al., 2017; Storey & Dalziel, 1987). While the lateral variation patterns are consistent, Shen et al. (2018) model slightly thicker crust at ~40–44 km beneath the Haag Nunataks and northern Ellsworth Mountains (Figure S6). Our inferred thickness of ~35–40 km along the imaged portion of the southern TAM is consistent with preceding receiver function studies (e.g., Chaput et al., 2014; Ramirez et al., 2017) but less than the ~35- to 48 km range inferred by Shen et al. (2018). The location of the southern TAM toward the periphery of our model where resolution degrades, coupled with the relatively high crustal thickness uncertainty along the TAM front acknowledged in Shen et al. (2018), likely contribute to this discrepancy.

Seismic refraction (Leitchenkov & Kudryavtzev, 1997) and gravity and magnetic data (Jordan et al., 2013; Jordan et al., 2017) suggest the presence of extensive underplating at the base of the crust in the Weddell Sea Rift System, which Jordan et al. (2017) attribute to plume-related Jurassic magmatism. O'Donnell et al. (2019) suggest that a subcrustal high shear wave velocity anomaly underlying the southern Weddell Sea Rift System might reflect depleted mantle lithosphere following the extraction of voluminous melt related to Gondwana breakup, that is, a fossil proto-Weddell plume signature. Our model suggests that the crust is ~30 km thick beneath the southern Weddell Sea Rift System between the Ellsworth Mountains and Dufek Intrusion (Figures 10 and 11), consistent with the ~28–32 km estimated by Shen et al. (2018). However, mafic underplate will smooth the impedance contrast between crust and mantle, rendering it difficult to differentiate between Scenarios (a) comparatively thicker crust with little or no underplate and (b) comparatively thinner crust with underplate. Acknowledging this fact, Jordan et al. (2013) model the crust beneath the inland extension of the Weddell Sea Rift as being either ~4 km thinner compared to the adjacent HEW block or as underlain by an up to 8-km-thick mafic underplate. Higher-resolution data are needed to unambiguously differentiate between Scenarios (a) and (b).

Because of the large impedance contrast at the Moho, lateral velocity variations at lower crustal and uppermost mantle depths typically correlate strongly with crustal thickness and, hence, tectonic block heritage. This spatial correlation weakens at midcrustal depths, with lateral variations in intracrustal structure instead coming to the fore (for example, compare  $V_{SV}$  maps at 12- and 28-km depth in Figure 9, also noting the contrasting color scale ranges). Although the sources of these anomalies lie closer to the Earth's surface, they are invariably more difficult to interpret. Subglacial sedimentary layers in the WARS have been inferred from receiver function analysis (e.g., Anandakrishnan & Winberry, 2004), and sediment thicknesses ranging up to several kilometres are reported for the Ross Sea Embayment (Lindeque et al., 2016, and references therein). Such sediment packages plausibly account for the regions of reduced  $V_{SV}$  velocity apparent within the WARS at, for example, 12 km depth in Figure 9. Cenozoic mafic crustal intrusions are another potential contributor to imaged seismic heterogeneity within the WARS. Such intrusions have been inferred in the Amundsen Sea Embayment from aerogravity data (Jordan et al., 2010). The  $V_{SV}$  velocities exceeding ~4.0 km/s at 20 km depth beneath the BSB and Ross Ice Shelf (Figure 9) may be the signature of rift-related lower crustal mafic intrusion. However, our seismic model is insufficient for their unambiguous detection.

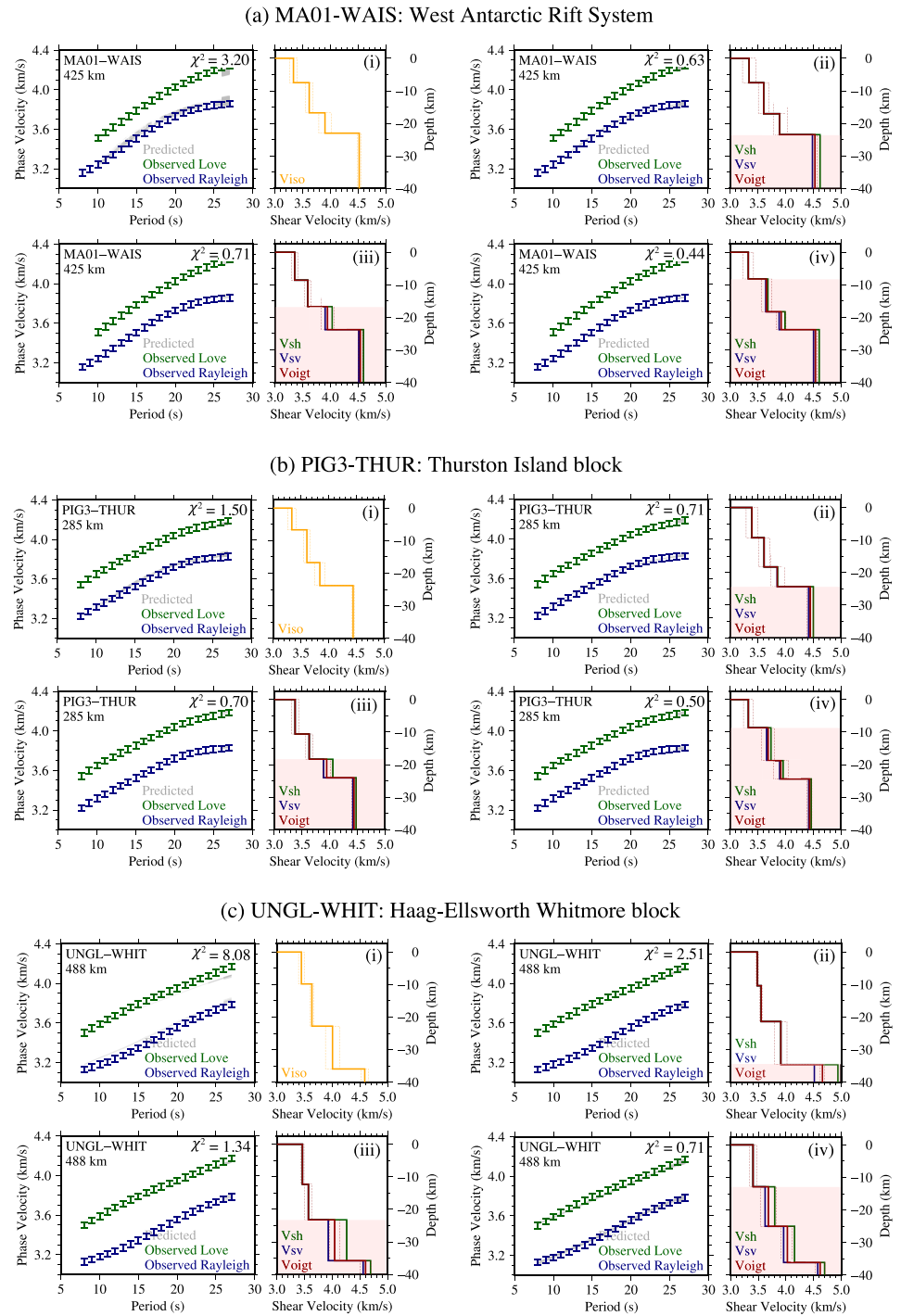


**Figure 12.**  $V_{SV}$ ,  $V_{SH}$ , Voigt average ( $= \sqrt{(V_{SH}^2 + 2V_{SV}^2)/3}$ ), and isotropic ( $V_{SV} = V_{SH} \equiv V_{ISO}$ ) interstation average velocity profiles for paths in central West Antarctica in the (a) West Antarctic Rift System, (b) Thurston Island block, and (c) Haag Nunataks-Ellsworth Whitmore block inferred from corresponding interstation Rayleigh and Love wave phase velocity dispersion curves. Dashed orange and red lines show one standard deviation bounds on the inferred isotropic and Voigt average shear wave velocity profiles. For each interstation path, four scenarios are considered: (i) isotropic uppermost mantle, isotropic crust; (ii) anisotropic uppermost mantle, isotropic crust; (iii) anisotropic uppermost mantle, anisotropic lower crust; and (iv) anisotropic uppermost mantle, anisotropic middle and lower crust (as a visual aid, permitted radially anisotropic layers are shaded). Predicted dispersion curves are shown in gray and corresponding  $\chi^2$  misfits denoted. Interstation distances are shown below the station pair labels. Figures S8, 13, and 14 map the corresponding inferred radial anisotropy strengths for Scenarios (ii), (iii), and (iv) for the ensemble of interstation paths for which both high-quality Rayleigh and Love wave dispersion data were available.



## 8. Radial Anisotropy

We now turn to the variation in crustal radial anisotropy between the crustal blocks of West Antarctica and assessment of the relative contributions of extensional deformation and structural or compositional layering to inferred anisotropy. Because the sparser ensemble of interstation Love wave measurements (Figure 5) was not conducive to a high-resolution tomography model, inference of radial anisotropy was confined to the ensemble of interstation paths for which both high-quality Rayleigh and Love wave dispersion data were available. The inferred  $V_{SV}$  and  $V_{SH}$  profiles subsequently shown thus represent 1-D average interstation velocity structure.

To facilitate testing of the depth extent of radial anisotropy, we used a simplified parameterization in which the crust was divided into upper, middle, and lower layers atop an uppermost mantle half-space. Upper, middle, and lower crustal layer thicknesses were permitted to vary between 4 and 15 km subject to the constraint that the combined thickness was within  $\pm 5$  km of interstation average crustal thickness estimates extracted from the An et al. (2015) Antarctic crustal model. Upper crustal  $V_{SV}$  was permitted to range from 3.2–3.5 km/s, middle crustal  $V_{SV}$  from 3.5–3.8 km/s, and lower crustal  $V_{SV}$  from 3.8–4.2 km/s, while the uppermost mantle  $V_{SV}$  was permitted to vary from 4.3–4.7 km/s. Shallow structure is not well constrained by the dispersion data, so the ice and upper crustal layers were modeled as isotropic.

Four scenarios are presented here: (i) isotropic uppermost mantle, isotropic crust; (ii) anisotropic uppermost mantle, isotropic crust; (iii) anisotropic uppermost mantle, anisotropic lower crust; and (iv) anisotropic uppermost mantle, anisotropic middle and lower crust. In each case radial anisotropy of up to  $\pm 10\%$  was permitted in anisotropic layers. However, when modeling more than one anisotropic layer we imposed the condition that the sign of radial anisotropy be the same in those layers (i.e., either all positive or all negative). This prevented negligible Rayleigh-Love discrepancies from being explained by the superposition and effective nullification of large positive and negative radial anisotropies in adjacent layers.

For dispersion curve prediction, vertically and horizontally polarized compressional wave velocities ( $V_{PV}$  and  $V_{PH}$ ) were scaled from inferred  $V_{SV}$  and  $V_{SH}$ , respectively, and densities from calculated isotropic average  $V_p$  velocities, using regressions from Brocher (2005). Following O'Donnell et al. (2017), we used genetic algorithm NSGA-II (Deb et al., 2002) to converge on the interstation 1-D average  $V_{SV}$  and  $V_{SH}$  models best explaining the interstation Rayleigh and Love wave dispersion data.

Figure 12 shows examples of 1-D  $V_{SV}$  and  $V_{SH}$  models for a selection of interstation paths in central West Antarctica encapsulated by, and representative of, parent crustal blocks (see Figure 1 for station locations). Upper, middle, and lower crustal layer thicknesses are generally stable between the four aforementioned modeling scenarios, and inferred crustal thicknesses are consistent with the patterns mapped in Figure 11. Improvements in resolving the Rayleigh-Love discrepancy (if evident) by introducing radial anisotropy are quantified by the reduced chi-square dispersion misfit ( $\chi^2 = n^{-1} \sum_{i=1}^n (d_i^{\text{obs}} - d_i^{\text{pre}})^2 \sigma_i^{-2}$ , where  $d_i^{\text{obs}}$  and  $d_i^{\text{pre}}$  are observed and predicted dispersion, respectively;  $n$  is the number of discrete dispersion measurements along the dispersion curves; and  $\sigma_i$  are uncertainties in the observed dispersion).

In relative terms, the interstation path in the HEW block (UNGL-WHIT; Figure 12c) shows the largest improvement in  $\chi^2$  misfit when radial anisotropy is permitted. Paths in the WARS (MA01-WAIS; Figure 12a) and Thurston Island block (PIG3-THUR; Figure 12b) show lesser, but still significant,  $\chi^2$  misfit improvements. Figure S7 shows the  $\chi^2$  misfit for the ensemble of viable interstation paths for the four inversion scenarios. The Rayleigh-Love discrepancy is almost everywhere reduced significantly going from the (i) isotropic uppermost mantle, isotropic crust regime to the (ii) anisotropic uppermost mantle, isotropic crust regime. Successive incremental reductions in the  $\chi^2$  misfits follow going from the (iii) anisotropic uppermost mantle, anisotropic lower-crust regime to the (iv) anisotropic uppermost mantle, anisotropic middle- and lower-crust regime, which yields the marginally lowest  $\chi^2$  misfit.

Figures S8, 13, and 14 map the corresponding inferred radial anisotropy strengths for Scenarios (ii), (iii), and (iv). The uncertainties are standard deviations derived from the final, best generations of models from the respective genetic algorithm searches. The modeled strength of radial anisotropy varies according to the number of layers over which it can be distributed. If confined to the uppermost mantle (Figure S8), modeled radial anisotropies along a number of paths exceed the  $\sim 3$ –6% strength range inferred for the West Antarctic uppermost mantle by Ritzwoller et al. (2001) and the global average value of  $\sim 4\%$  near the top of the mantle

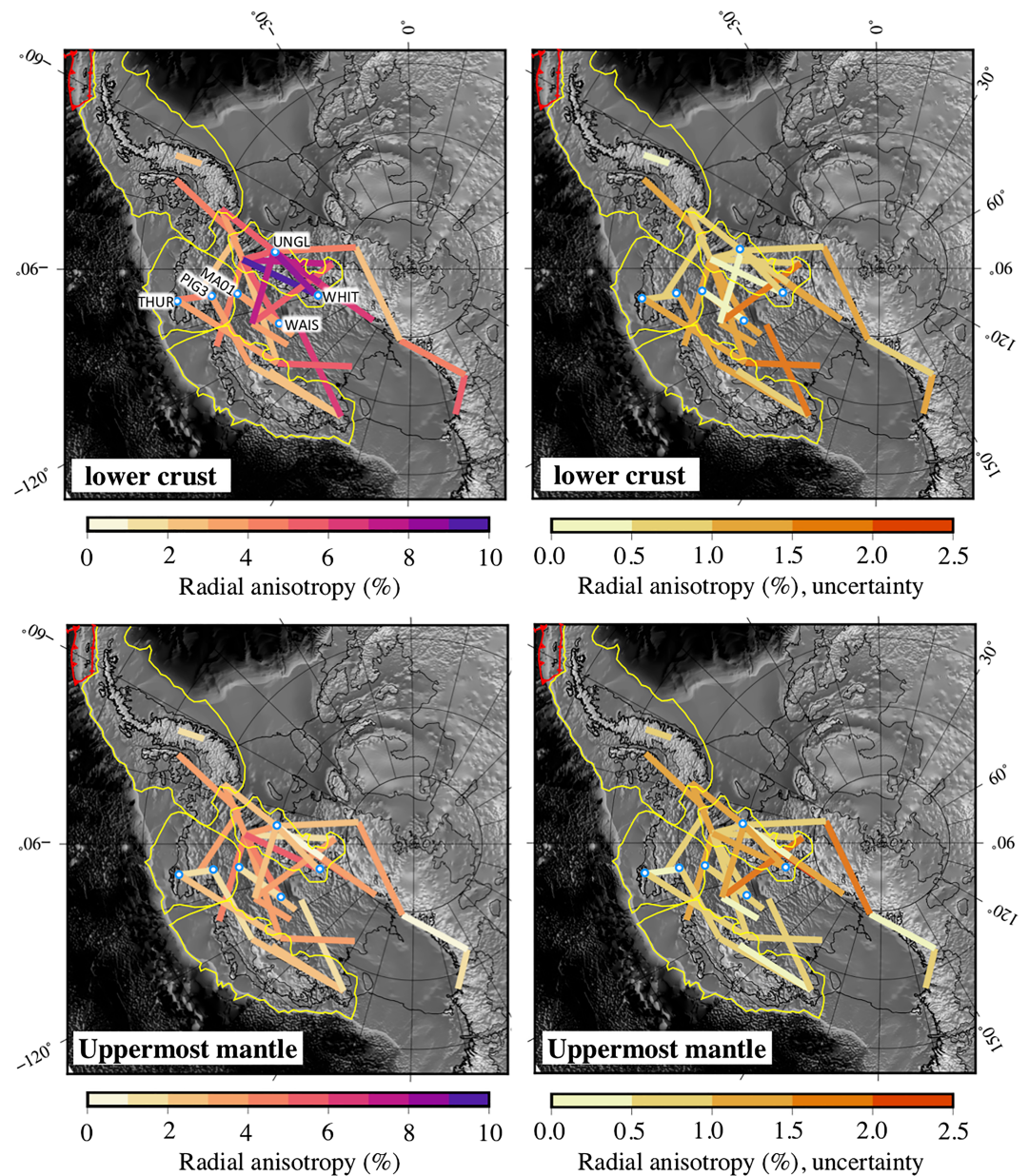


**Figure 13.** Interstation average percent radial anisotropy resolving the Rayleigh-Love discrepancy (if any) for Scenario (iii) anisotropic uppermost mantle and anisotropic lower crust. The uncertainties are standard deviations derived from the final, best generations of anisotropic models from the genetic algorithm searches. The stations labeled are those shown in Figure 12.

reported by Shapiro and Ritzwoller (2002). Permitting anisotropy in the crust (Figures 13 and 14) reduces the modeled strength of radial anisotropy in the uppermost mantle to an average of ~3–4%, values in line with Ritzwoller et al. (2001) and Shapiro and Ritzwoller (2002). While the (iv) anisotropic uppermost mantle, anisotropic middle- and lower-crust regime yields marginally lower  $\chi^2$  misfits than the (iii) anisotropic uppermost mantle, anisotropic lower-crust regime (Figure S7), without independent constraints we cannot unambiguously claim that (iv) best represents reality.

Although our Love dispersion data have limited sensitivity to uppermost mantle structure (Figure 4), confining radial anisotropy to the crust (i.e., isotropic uppermost mantle) necessitates much stronger radial anisotropy (up to ~15%) to explain the Rayleigh-Love discrepancies to comparable  $\chi^2$  misfits (Figure S9). Crustal radial anisotropy of this magnitude (up to ~15%) significantly exceeds magnitudes inferred in the

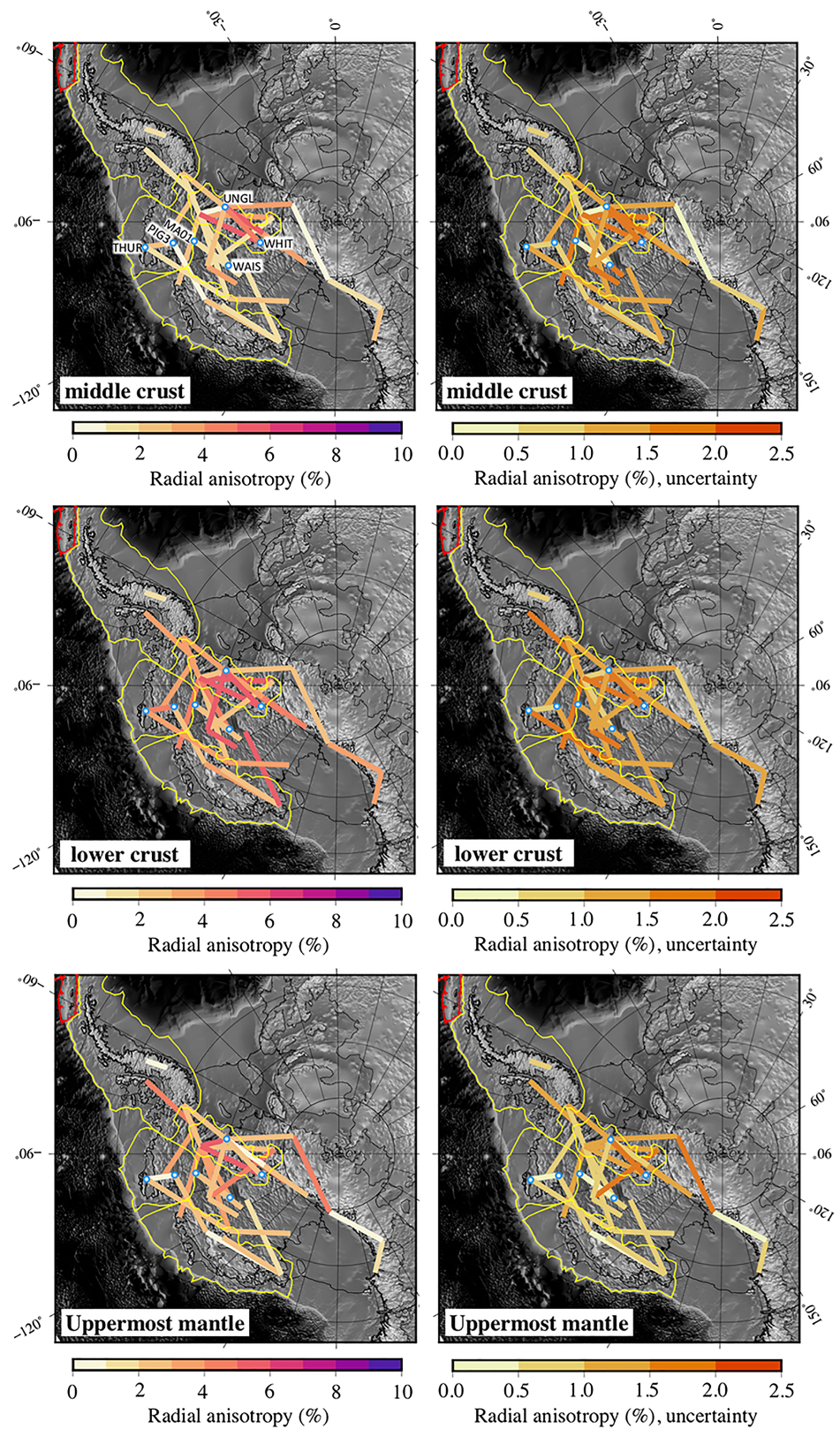


**Figure 14.** Interstation average percent radial anisotropy resolving the Rayleigh-Love discrepancy (if any) for Scenario (iv) anisotropic uppermost mantle and anisotropic middle and lower crust. The uncertainties are standard deviations derived from the final, best generations of anisotropic models from the genetic algorithm searches. The stations labeled are those shown in Figure 12.

middle to lower crust in Cenozoic ( $>5\%$ , Moschetti et al., 2010) and Mesozoic (4–6%, Guo, Yang, et al., 2016) extensional provinces in the western United States and northeast China, respectively, and in the middle crust of ancient cratonic and adjacent transitional craton-to-cordillera terranes in northwestern Canada ( $\sim 4\text{--}5\%$ ; Dalton & Gaherty, 2013). In our case, simultaneously modeling a radially anisotropic uppermost mantle results in anisotropy strengths consistent with existing estimates of crustal (e.g., Dalton & Gaherty, 2013; Guo, Yang, et al., 2016; Moschetti et al., 2010) and uppermost mantle (e.g., Ritzwoller et al., 2001; Shapiro & Ritzwoller, 2002) radial anisotropy strength.

### 8.1. Tectonic Interpretation of Radial Anisotropy Variations

Drawing on both modeling Scenarios (iii) and (iv) (Figures 13 and 14), we can make several robust inferences on the lateral variations in crustal radial anisotropy strength across West Antarctica. Overall, the models suggest that the lower crust and potentially the middle crust is positively radially anisotropic across West Antarctica. The HEW block exhibits the strongest radial anisotropy: up to  $8\text{--}10\pm 1\%$  if confined to a lower crustal layer, and  $4\text{--}6\pm 2\%$  if distributed over middle and lower crustal layers. Positive radial anisotropy of  $\sim 3\text{--}7\pm 2\%$  in the lower crustal layer and  $\sim 1\text{--}3\pm 1.5\%$  in the middle crustal layer is generally characteristic of paths outside the HEW block. While acknowledging the limited geographical coverage provided by the selected interstation paths, the HEW block aside, no significant contrast in radial anisotropy strength between the other tectonic blocks of West Antarctica is discernible. This emphasizes the unique tectonic structure and provenance of the HEW block among the West Antarctic crustal units.

Dalton and Gaherty (2013) attributed  $\sim 4\text{--}5\%$  positive middle crustal radial anisotropy in northwestern Canada to metamorphic assemblages in cratonic crust and to a thick, layered metasedimentary package in an adjacent transitional craton-to-cordillera terrane. The HEW block exposes a  $\sim 13\text{-km}$ -thick stratigraphic succession of Paleozoic metasedimentary and volcanic rocks in the Ellsworth Whitmore Mountains, and Precambrian basement dated to  $\sim 1$  Ga in the Haag Nunataks (e.g., Curtis, 2001; Jordan et al., 2017; Storey & Kyle, 1997, and references therein). While our modeling cannot disentangle any contribution rooted in fabric developed by past deformation and/or translation of the block, following Dalton and Gaherty (2013), the  $\sim 13\text{-km}$ -thick metasedimentary succession atop Precambrian metamorphic basement conceivably accounts for the pronounced radial anisotropy modeled in the HEW block.

Positive radial anisotropy in the WARS crust ( $\sim 3\text{--}7\pm 2\%$  in the lower crustal layer and  $\sim 1\text{--}3\pm 1.5\%$  in the middle crustal layer) is consistent with the observation of positive radial anisotropy in the middle to lower crust in other extensional settings (e.g., Guo, Yang, et al., 2016; Moschetti et al., 2010). The lattice-preferred orientation of minerals such as mica and amphibole by extensional deformation is a feasible explanatory mechanism (e.g., Godfrey et al., 2000; Ko & Jung, 2015; Siegesmund et al., 1989; Tatham et al., 2008; Weiss et al., 1999). The limited interstation path coverage precludes robust identification and delineation of differential extension within the WARS.

The paths either partially or wholly within the MBL, Thurston Island and Antarctic Peninsula crustal blocks are either close to the WARS margin or cross inferred zones of extension. Lattice-preferred orientation of anisotropic minerals by extensional deformation might also then explain the modeled positive crustal radial anisotropy along these paths ( $\sim 3\text{--}5\pm 2\%$  in the lower crustal layer and  $\sim 1\text{--}3\pm 1.5\%$  in the middle crustal layer). However, following Dalton and Gaherty (2013), the observation of radial anisotropy in the MBL, Thurston Island, and Antarctic Peninsula crustal blocks might also reflect the ubiquity of anisotropy in continental crust.

## 9. Conclusions

Using seismic data from the UKANET and POLENET-ANET arrays, we extracted Rayleigh and Love wave phase velocity dispersion data at periods 8–25 s from ambient noise cross correlograms to (i) map the 3-D  $V_{SV}$  structure of the West Antarctic crust—including a crustal thickness map determined from the initial instance in depth of  $V_{SV} > 4.3$  km/s - and (ii) probe for middle to lower crustal and uppermost mantle radial anisotropy.

The thinnest WARS crust ( $\sim 22$  km thick) modeled occurs beneath the Ross Ice Shelf and in the vicinity of the BSB in the Amundsen Sea Embayment. In the WARS, a ridge of  $\sim 26\text{--}30\text{-km}$ -thick crust extending south across from the MBL topographic dome separates the domains of more extended crust in the Ross and

Amundsen Sea Embayments (Figure 11). If distributed Cretaceous rifting thinned the WARS crust from  $\sim 35$  to  $\sim 26$  km (e.g., Jordan et al., 2010), this ridge of thicker crust suggests that Cenozoic rifting was not uniform across the WARS, assuming that crustal thickness was similar everywhere in the WARS prior to rifting. Instead, our  $V_{SV}$  model suggests that Cenozoic rifting was concentrated in the Ross Sea and Amundsen Sea Embayments. This points to along-strike variability in the Cenozoic evolution of the WARS with implications for global plate circuit modeling.

The southern margin of the WARS is defined along the southern TAM and HEW block by a sharp crustal thickness gradient (Figures 10 and 11). Our model suggests that the southern WARS margin continues striking toward the Bellinghousen Sea, coincident with the common boundary of the HEW, Thurston Island, and Antarctic Peninsula crustal blocks.

The thickest crust ( $\sim 35$ – $40$  km) is modeled beneath the southern TAM and Haag Nunataks-Ellsworth Mountains (Figures 10 and 11). The  $\sim 35$ - to  $40$ -km-thick crust inferred beneath the Haag Nunataks and northern Ellsworth Mountains decreases to a thickness of  $\sim 30$ – $32$  km beneath the Whitmore Mountains, a trend consistent with the recognition of distinct structural domains within the composite HEW block (e.g., Jordan et al., 2017; Storey & Dalziel, 1987).

In MBL, the general pattern is of crustal thickness increasing northward from  $\sim 28$ – $30$  at the southern margin of the block to  $\sim 35$ – $38$  km in the block interior (Figures 10 and 11). According to the West Antarctic crustal block boundaries from Dalziel and Elliot (1982), we model  $\sim 26$ -km-thick crust at the eastern end of the MBL block within the Amundsen Sea Embayment. Using the revision to the MBL block boundary as suggested by Damiani et al. (2014), much of this region of  $\sim 26$  km crust is instead designated part of the WARS, supporting the suggested revision (Figure 11).

Our model suggests that the crust is  $\sim 30$  km thick beneath the southern Weddell Sea Rift System between the Ellsworth Mountains and Dufek Intrusion. However, we are unable to disentangle from the thickness estimate a potential contribution of putative underplate related to the Jurassic development of the rift system (e.g., Jordan et al., 2013).

To probe seismic anisotropy, we modeled 1-D average interstation  $V_{SV}$  and  $V_{SH}$  structure along paths for which both high-quality Rayleigh and Love wave phase velocity dispersion data were available. Our modeling suggests that the lower crust and possibly the middle crust is positively radially anisotropic ( $V_{SH} > V_{SV}$ ) across West Antarctica.

The HEW block exhibits the strongest crustal radial anisotropy: up to  $8$ – $10 \pm 1\%$  if confined to a lower crustal layer, and  $4$ – $6 \pm 2\%$  if distributed over middle and lower crustal layers. Positive radial anisotropy of  $\sim 3$ – $7 \pm 2\%$  in the lower crustal layer and  $\sim 1$ – $3 \pm 1.5\%$  in the middle crustal layer is generally characteristic of paths outside the HEW block (Figures 13 and 14). While acknowledging the limited geographical coverage of our modeling, the HEW block aside, no significant contrast in radial anisotropy strength between the other tectonic blocks of West Antarctica is discernible. This emphasizes the unique provenance of the HEW block among the West Antarctic crustal units. Following Dalton and Gaherty (2013), the  $\sim 13$ -km-thick metasedimentary succession exposed in the Ellsworth Mountains atop Precambrian metamorphic basement (e.g., Curtis, 2001; Jordan et al., 2017; Storey & Kyle, 1997, and references therein) conceivably accounts for the pronounced radial anisotropy modeled in the HEW block.

Positive radial anisotropy in the WARS crust ( $\sim 3$ – $7 \pm 2\%$  in the lower crustal layer and  $\sim 1$ – $3 \pm 1.5\%$  in the middle crustal layer) is consistent with the observation of positive radial anisotropy in the middle to lower crust in other Mesozoic and Cenozoic extensional settings (e.g., Guo, Yang, et al., 2016; Moschetti et al., 2010). The lattice-preferred orientation of minerals such as mica and amphibole by extensional deformation is a feasible explanatory mechanism (e.g., Godfrey et al., 2000; Ko & Jung, 2015; Siegesmund et al., 1989; Tatham et al., 2008; Weiss et al., 1999). Lattice-preferred orientation through extensional deformation might also explain positive crustal radial anisotropy ( $\sim 3$ – $5 \pm 2\%$  in the lower crustal layer and  $\sim 1$ – $3 \pm 1.5\%$  in the middle crustal layer) along paths in the MBL, Thurston Island, and Antarctic Peninsula crustal blocks that are either close to the WARS margin or cross inferred zones of extension. Alternatively, these paths might reflect the proposed ubiquity of anisotropy in continental crust (Dalton & Gaherty, 2013).

**Acknowledgments**

We thank all BAS camp staff, field guides, and air unit personnel for the logistical support of the UKANET seismic and GNSS networks. We similarly acknowledge all field teams and camp staff associated with the POLENET-ANET project and thank Kenn Borek Air and the New York Air Guard for flight support. J. P. O. D., C. K. D., G. A. N., and P. L. W. are supported by the Natural Environment Research Council (Grants NE/L006065/1, NE/L006294/1, and NE/K009958/1). POLENET-ANET is supported by the National Science Foundation Office of Polar Programs (Grants 0632230, 0632239, 0652322, 0632335, 0632136, 0632209, and 0632185). UKANET seismic instrumentation was provided and supported by SEIS-UK. POLENET-ANET seismic instrumentation was provided and supported by the Incorporated Research Institutions for Seismology (IRIS) through the PASSCAL Instrument Center. The UKANET ([www.ukanet.wixsite.com/ukanet](http://www.ukanet.wixsite.com/ukanet); network code 1D; [https://doi.org/10.7914/SN/1D\\_2016](https://doi.org/10.7914/SN/1D_2016)) data will be accessible through the IRIS Data Management Center (<http://www.iris.edu/mda>) from January 2021. POLENET-ANET (network code YT), ASAIN (network code AI), GSN (network code IU), and SEPA (network code XB) seismic data can be accessed through the IRIS DMC. The facilities of the IRIS Consortium are supported by the NSF under cooperative Agreement EAR-1063471, the NSF Office of Polar Programs, and the DOE National Nuclear Security Administration. Figures were created using the Generic Mapping Tools (GMT) software (Wessel & Smith, 1998) with color maps from Kovesi (2015) and Cramer (2018). The phase and shear wave velocity models developed here can be accessed at the UK Polar Data Centre, <https://doi.org/10.5285/b5ffac8a-9846-4f86-9a71-3ce992a18148>. We thank Simone Pilia and an anonymous reviewer for reviews.

**References**

An, M., Wiens, D. A., Zhao, Y., Feng, M., Nyblade, A. A., Kanao, M., et al. (2015). S-velocity model and inferred Moho topography beneath the Antarctic Plate from Rayleigh waves. *Journal of Geophysical Research: Solid Earth*, *120*, 359–383. <https://doi.org/10.1002/2014JB011332>

Anandakrishnan, S., & Winberry, J. (2004). Antarctic subglacial sedimentary layer thickness from receiver function analysis. *Global and Planetary Change*, *42*(1-4), 167–176.

Bensen, G. D., Ritzwoller, M. H., Barmin, M. P., Levshin, A. L., Lin, F., Moschetti, M. P., et al. (2007). Processing seismic ambient noise data to obtain reliable broad-band surface wave dispersion measurements. *Geophysical Journal International*, *169*(3), 1239–1260. <https://doi.org/10.1111/j.1365-246X.2007.03374.x>

Brisbourne, A., Stuart, G., & O'Donnell, J. P. (2016). UKANET: UK Antarctic Network, International Federation of Digital Seismograph Networks. Dataset/Seismic Network. [https://doi.org/10.7914/SN/1D\\_2016](https://doi.org/10.7914/SN/1D_2016)

Brocher, T. M. (2005). Empirical relations between elastic wavespeeds and density in the Earth's crust. *Bulletin of the Seismological Society of America*, *95*(6), 2081.

Campillo, M., & Paul, A. (2003). Long-range correlations in the diffuse seismic coda. *Science*, *299*(5606), 547–549.

Cande, S. C., Stock, J. M., Müller, R. D., & Ishihara, T. (2000). Cenozoic motion between East and West Antarctica. *Nature*, *404*(6774), 145.

Chaput, J., Aster, R. C., Huerta, A., Sun, X., Lloyd, A., Wiens, D., et al. (2014). The crustal thickness of West Antarctica. *Journal of Geophysical Research: Solid Earth*, *119*, 1–18. <https://doi.org/10.1002/2013JB010642>

Crameri, F. (2018). Geodynamic diagnostics, scientific visualisation and StagLab 3.0. *Geoscientific Model Development*, *11*(6), 2541–2562. <https://doi.org/10.5194/gmd-11-2541-2018>

Curtis, M. L. (2001). Tectonic history of the Ellsworth Mountains, West Antarctica: Reconciling a Gondwana enigma. *GSA Bulletin*, *113*(7), 939–958.

Dalton, C. A., & Gaherty, J. B. (2013). Seismic anisotropy in the continental crust of northwestern Canada. *Geophysical Journal International*, *193*(1), 338–348. <https://doi.org/10.1093/gji/ggs108>

Dalziel, I. W. D. (1992). Antarctica: A tale of two supercontinents? *Annual Review of Earth and Planetary Sciences*, *20*, 501–526.

Dalziel, I. W. D., & Elliot, D. H. (1982). West Antarctica: Problem child of Gondwanaland. *Tectonics*, *1*, 3–19. <https://doi.org/10.1029/TC001i001p00003>

Damiani, T. M., Jordan, T. A., Ferraccioli, F., Young, D. A., & Blankenship, D. D. (2014). Variable crustal thickness beneath Thwaites Glacier revealed from airborne gravimetry, possible implications for geothermal heat flux in West Antarctica. *Earth and Planetary Science Letters*, *407*, 109–122. <https://doi.org/10.1016/j.epsl.2014.09.023>

Davey, F. J., Cande, S. C., & Stock, J. M. (2006). Extension in the western Ross Sea region-links between Adare Basin and Victoria Land Basin. *Geophysical Research Letters*, *33*, L20315. <https://doi.org/10.1029/2006GL027383>

Deb, K., Pratap, A., Agarwal, S., & Meyarivan, T. (2002). A fast and elitist multiobjective genetic algorithm: NSGA-II. *IEEE Transactions on Evolutionary Computation*, *6*(2), 182–197.

Divenere, V., Kent, D. V., & Dalziel, I. W. D. (1996). Summary of palaeomagnetic results from West Antarctica: Implications for the tectonic evolution of the Pacific margin of Gondwana during the Mesozoic. *Geological Society London Special Publications*, *108*(1), 31–43. <https://doi.org/10.1144/GSL.SP.1996.108.01.03>

Dziewonski, A. M., & Anderson, D. L. (1981). Preliminary reference Earth model. *Physics of the Earth and Planetary Interiors*, *25*(4), 297–356.

Dziewonski, A., Bloch, S., & Landisman, M. (1969). A technique for the analysis of transient seismic signals. *Bulletin of the Seismological Society of America*, *59*(1), 427.

Ekström, G., Abers, G. A., & Webb, S. C. (2009). Determination of surface-wave phase velocities across USArray from noise and Aki's spectral formulation. *Geophysical Research Letters*, *36*, L18301. <https://doi.org/10.1029/2009GL039131>

Elliot, D. H., & Fleming, T. H. (2000). Weddell triple junction: The principal focus of Ferrar and Karoo magmatism during initial breakup of Gondwana. *Geology*, *28*(6), 539.

Ferris, J. K., Vaughan, A. P. M., & Storey, B. C. (2000). Relics of a complex triple junction in the Weddell Sea embayment, Antarctica. *Earth and Planetary Science Letters*, *178*(3), 215–230. [https://doi.org/10.1016/S0012-821X\(00\)00076-5](https://doi.org/10.1016/S0012-821X(00)00076-5)

Finn, C. A., Müller, R. D., & Panter, K. S. (2005). A Cenozoic diffuse alkaline magmatic province (DAMP) in the southwest Pacific without rift or plume origin. *Geochemistry, Geophysics, Geosystems*, *6*, Q02005. <https://doi.org/10.1029/2004GC000723>

Fitzgerald, P. (2002). Tectonics and landscape evolution of the Antarctic plate since the breakup of Gondwana, with an emphasis on the West Antarctic Rift System and the Transantarctic Mountains. *Royal Society of New Zealand Bulletin*, *35*, 453–469.

Fretwell, P., Pritchard, H. D., Vaughan, D. G., Bamber, J. L., Barrand, N. E., Bell, R., et al. (2013). Bedmap2: Improved ice bed, surface and thickness datasets for Antarctica. *The Cryosphere*, *7*, 375–393. <https://doi.org/10.5194/tc-7-375-2013>

Godfrey, N. J., Christensen, N. I., & Okaya, D. A. (2000). Anisotropy of schists: Contribution of crustal anisotropy to active source seismic experiments and shear wave splitting observations. *Journal of Geophysical Research*, *105*, 27,991–28,007. <https://doi.org/10.1029/2000JB900286>

Granot, R., & Dymet, J. (2018). Late Cenozoic unification of East and West Antarctica. *Nature Communications*, *9*(1), 3189.

Guo, Z., Chen, Y. J., Ning, J., Yang, Y., Afonso, J. C., & Tang, Y. (2016). Seismic evidence of on-going sublithosphere upper mantle convection for intra-plate volcanism in Northeast China. *Earth and Planetary Science Letters*, *433*, 31–43.

Guo, Z., Yang, Y., & Chen, Y. J. (2016). Crustal radial anisotropy in northeast China and its implications for the regional tectonic extension. *Geophysical Journal International*, *207*(1), 197–208.

Haario, H., Laine, M., Mira, A., & Saksman, E. (2006). DRAM: Efficient adaptive MCMC. *Statistics and Computing*, *16*(4), 339–354.

Heeszel, D. S., Wiens, D. A., Anandakrishnan, S., Aster, R. C., Dalziel, I. W. D., Huerta, A. D., et al. (2016). Upper mantle structure of central and West Antarctica from array analysis of Rayleigh wave phase velocities. *Journal of Geophysical Research: Solid Earth*, *121*, 1758–1775. <https://doi.org/10.1002/2015JB012616>

Holbrook, WSTEVEN, Mooney, W. D., & Christensen, N. I. (1992). The seismic velocity structure of the deep continental crust. *Continental lower crust*, *23*, 1–43.

Johnson, J. S., O'Donnell, J. P., & Thomas, E. R. (2018). In situ measurements of snow accumulation in the Amundsen Sea Embayment during 2016. *Antarctic Science*, *30*(3), 197–203. <https://doi.org/10.1017/S0954102018000068>

Jordan, T. A., Ferraccioli, F., & Leat, P. T. (2017). New geophysical compilations link crustal block motion to Jurassic extension and strike-slip faulting in the Weddell Sea Rift System of West Antarctica. *Gondwana Research*, *42*, 29–48. <https://doi.org/10.1016/j.gr.2016.09.009>

- Jordan, T. A., Ferraccioli, F., Ross, N., Corr, H. F. J., Leat, P. T., Bingham, R. G., et al. (2013). Inland extent of the Weddell Sea Rift imaged by new aerogeophysical data. *Tectonophysics*, 585, 137–160. <https://doi.org/10.1016/j.tecto.2012.09.010>
- Jordan, T. A., Ferraccioli, F., Vaughan, D. G., Holt, J. W., Corr, H., Blankenship, D. D., & Diehl, T. M. (2010). Aerogravity evidence for major crustal thinning under the Pine Island Glacier region (West Antarctica). *GSA Bulletin*, 122(5–6), 714. <https://doi.org/10.1130/B26417.1>
- Kennett, B. L. N., Engdahl, E. R., & Buland, R. (1995). Constraints on seismic velocities in the Earth from traveltimes. *Geophysical Journal International*, 122(1), 108–124. <https://doi.org/10.1111/j.1365-246X.1995.tb03540.x>
- Kennett, B. L. N., Sambridge, M. S., & Williamson, P. R. (1988). Subspace methods for large inverse problems with multiple parameter classes. *Geophysical Journal International*, 94(2), 237–247. <https://doi.org/10.1111/j.1365-246X.1988.tb05898.x>
- Ko, B., & Jung, H. (2015). Crystal preferred orientation of an amphibole experimentally deformed by simple shear. *Nature Communications*, 6, 6586. <https://doi.org/10.1038/ncomms7586>
- Kovesi, P. (2015). Good colour maps: How to design them. arXiv preprint arXiv:1509.03700.
- Lawver, L. A., & Gahagan, L. M. (1994). Constraints on timing of extension in the Ross Sea region. *Terra Antarctica*, 1(3), 545–552.
- LeMasurier, W. E. (2008). Neogene extension and basin deepening in the West Antarctic rift inferred from comparisons with the East African rift and other analogs. *Geology*, 36(3), 247–250.
- LeMasurier, W. E., & Landis, C. A. (1996). Mantle-plume activity recorded by low-relief erosion surfaces in West Antarctica and New Zealand. *Geological Society of America Bulletin*, 108(11), 1450–1466.
- Leitchenkov, G. L., & Kudryavtzev, G. A. (1997). Structure and origin of the Earth's crust in the Weddell Sea embayment (beneath the front of the Filchner and Ronne Ice Shelves) from deep seismic sounding data. *Polarforschung*, 67(3), 143–154.
- Levshin, A. L., & Ritzwoller, M. H. (2001). Automated detection, extraction, and measurement of regional surface waves. *Pure and Applied Geophysics*, 158(8), 1531–1545.
- Lin, F.-C., Moschetti, M. P., & Ritzwoller, M. H. (2008). Surface wave tomography of the western United States from ambient seismic noise: Rayleigh and Love wave phase velocity maps. *Geophysical Journal International*, 173(1), 281–298.
- Lin, F.-C., Ritzwoller, M. H., & Snieder, R. (2009). Eikonal tomography: Surface wave tomography by phase front tracking across a regional broad-band seismic array. *Geophysical Journal International*, 177(3), 1091–1110. <https://doi.org/10.1111/j.1365-246X.2009.04105.x>
- Linde, A., Gohl, K., Wobbe, F., & Uenzelmann-Neben, G. (2016). Preglacial to glacial sediment thickness grids for the southern Pacific margin of West Antarctica. *Geochemistry, Geophysics, Geosystems*, 17, 4276–4285. <https://doi.org/10.1002/2016GC006401>
- Lloyd, A. J., Wiens, D. A., Nyblade, A. A., Anandkrishnan, S., Aster, R. C., Huerta, A. D., et al. (2015). A seismic transect across West Antarctica: Evidence for mantle thermal anomalies beneath the Bentley Subglacial Trench and the Marie Byrd Land Dome. *Journal of Geophysical Research: Solid Earth*, 120, 8439–8460. <https://doi.org/10.1002/2015JB012455>
- Long, M. D., & Silver, P. G. (2009). Shear wave splitting and mantle anisotropy: Measurements, interpretations, and new directions. *Surveys in Geophysics*, 30(4), 407–461. <https://doi.org/10.1007/s10712-009-9075-1>
- Masters, G., Woodhouse, J. H., & Freeman, J. H. (2011). Mineos v1.0.2 [software]. Computational infrastructure for geodynamics, <https://geodynamics.org/cig/software/mineos/>.
- Moschetti, M. P., Ritzwoller, M. H., Lin, F.-C., & Yang, Y. (2010). Seismic evidence for widespread western-US deep-crustal deformation caused by extension. *Nature*, 464(7290), 885.
- Müller, R. D., Gohl, K., Cande, S. C., Goncharov, A., & Golynsky, A. V. (2007). Eocene to Miocene geometry of the West Antarctic Rift System. *Australian Journal of Earth Sciences*, 54(8), 1033–1045. <https://doi.org/10.1080/08120090701615691>
- O'Donnell, J. P., & Nyblade, A. A. (2014). Antarctica's hypsometry and crustal thickness: Implications for the origin of anomalous topography in East Antarctica. *Earth and Planetary Science Letters*, 388, 143–155.
- O'Donnell, J. P., Selway, K., Nyblade, A. A., Brazier, R. A., Wiens, D. A., Anandkrishnan, S., et al. (2017). The uppermost mantle seismic velocity and viscosity structure of central West Antarctica. *Earth and Planetary Science Letters*, 472, 38–49. <https://doi.org/10.1016/j.epsl.2017.05.016>
- O'Donnell, J. P., Stuart, G. W., Brisbourne, A. M., Selway, K., Yang, Y., Nield, G. A., et al. (2019). The uppermost mantle seismic velocity structure of West Antarctica from Rayleigh wave tomography: Insights into tectonic structure and geothermal heat flow. *Earth and Planetary Science Letters*, 522, 219–233. <https://doi.org/10.1016/j.epsl.2019.06.024>
- Pappa, F., Ebbing, J., & Ferraccioli, F. (2019). Moho Depths of Antarctica: Comparison of seismic, gravity, and isostatic results. *Geochemistry, Geophysics, Geosystems*, 20, 1629–1645. <https://doi.org/10.1029/2018GC008111>
- Pilia, S., Arroucau, P., Rawlinson, N., Reading, A. M., & Cayley, R. A. (2016). Inherited crustal deformation along the East Gondwana margin revealed by seismic anisotropy tomography. *Geophysical Research Letters*, 43, 12,082–12,090. <https://doi.org/10.1002/2016GL071201>
- Pyle, M. L., Wiens, D. A., Nyblade, A. A., & Anandkrishnan, S. (2010). Crustal structure of the Transantarctic Mountains near the Ross Sea from ambient seismic noise tomography. *Journal of Geophysical Research*, 115, B11310. <https://doi.org/10.1029/2009JB007081>
- Rabbel, W., & Mooney, W. D. (1996). Seismic anisotropy of the crystalline crust: What does it tell us? *Terra Nova*, 8(1), 16–21. <https://doi.org/10.1111/j.1365-3121.1996.tb00721.x>
- Ramirez, C., Nyblade, A., Emry, E. L., Julià, J., Sun, X., Anandkrishnan, S., et al. (2017). Crustal structure of the Transantarctic Mountains, Ellsworth Mountains and Marie Byrd Land, Antarctica: Constraints on shear wave velocities, Poisson's ratios and Moho depths. *Geophysical Journal International*, 211(3), 1328–1340.
- Ramirez, C., Nyblade, A., Hansen, S. E., Wiens, D. A., Anandkrishnan, S., Aster, R. C., et al. (2016). Crustal and upper-mantle structure beneath ice-covered regions in Antarctica from S-wave receiver functions and implications for heat flow. *Geophysical Journal International*, 204(3), 1636–1648.
- Rawlinson, N., & Sambridge, M. (2004). Multiple reflection and transmission phases in complex layered media using a multistage fast marching method. *Geophysics*, 69(5), 1338–1350. <https://doi.org/10.1190/1.1801950>
- Rawlinson, N., & Sambridge, M. (2005). The fast marching method: An effective tool for tomographic imaging and tracking multiple phases in complex layered media. *Exploration Geophysics*, 36(4), 341–350.
- Reading, A. M. (2007). The seismicity of the Antarctic plate. *Geological Society of America Special Papers*, 425, 285–298. [https://doi.org/10.1130/2007.2425\(18\)](https://doi.org/10.1130/2007.2425(18))
- Ren, Y., Grecu, B., Stuart, G., Houseman, G., Hegedüs, E., & South Carpathian Project Working Group (2013). Crustal structure of the Carpathian-Pannonian region from ambient noise tomography. *Geophysical Journal International*, 195(2), 1351–1369.
- Rhie, J., & Romanowicz, B. (2004). Excitation of Earth's continuous free oscillations by atmosphere-ocean-seafloor coupling. *Nature*, 431(7008), 552.
- Ritzwoller, M. H., Shapiro, N. M., Levshin, A. L., & Leahy, G. M. (2001). Crustal and upper mantle structure beneath Antarctica and surrounding oceans. *Journal of Geophysical Research*, 106, 30,645–30,670. <https://doi.org/10.1029/2001JB000179>
- Savage, M. K. (1999). Seismic anisotropy and mantle deformation: What have we learned from shear wave splitting? *Reviews of Geophysics*, 37(1), 65–106. <https://doi.org/10.1029/98RG02075>

- Schimmel, M. (1999). Phase cross-correlations: Design, comparisons, and applications. *Bulletin of the Seismological Society of America*, 89(5), 1366.
- Schimmel, M., & Gallart, J. (2007). Frequency-dependent phase coherence for noise suppression in seismic array data. *Journal of Geophysical Research*, 112, B04303. <https://doi.org/10.1029/2006JB004680>
- Schimmel, M., Stutzmann, E., & Gallart, J. (2011). Using instantaneous phase coherence for signal extraction from ambient noise data at a local to a global scale. *Geophysical Journal International*, 184(1), 494–506.
- Sethian, J. A., & Popovici, A. M. (1999). 3-D traveltimes computation using the fast marching method. *Geophysics*, 64(2), 516–523. <https://doi.org/10.1190/1.1444558>
- Shan, B., Afonso, J. C., Yang, Y., Grose, C. J., Zheng, Y., Xiong, X., & Zhou, L. (2014). The thermochemical structure of the lithosphere and upper mantle beneath south China: Results from multiobservable probabilistic inversion. *Journal of Geophysical Research: Solid Earth*, 119, 8417–8441. <https://doi.org/10.1002/2014JB011412>
- Shapiro, N. M., Campillo, M., Stehly, L., & Ritzwoller, M. H. (2005). High-resolution surface-wave tomography from ambient seismic noise. *Science*, 307(5715), 1615–1618.
- Shapiro, N. M., & Ritzwoller, M. H. (2002). Monte-Carlo inversion for a global shear-velocity model of the crust and upper mantle. *Geophysical Journal International*, 151(1), 88–105. <https://doi.org/10.1046/j.1365-246X.2002.01742.x>
- Shen, W., Wiens, D. A., Anandakrishnan, S., Aster, R. C., Gerstoft, P., Bromirski, P. D., et al. (2018). The crust and upper mantle structure of central and West Antarctica from Bayesian inversion of Rayleigh wave and receiver functions. *Journal of Geophysical Research: Solid Earth*, 123, 7824–7849. <https://doi.org/10.1029/2017JB015346>
- Siddoway, C. S. (2008). Tectonics of the West Antarctic Rift System: New light on the history and dynamics of distributed intracontinental extension. *Antarctica: A Keystone in a Changing World*, 91–114.
- Siegesmund, S., Takeshita, T., & Kern, H. (1989). Anisotropy of  $V_p$  and  $V_s$  in an amphibolite of the deeper crust and its relationship to the mineralogical, microstructural and textural characteristics of the rock. *Tectonophysics*, 157, 25–38. [https://doi.org/10.1016/0040-1951\(89\)90338-7](https://doi.org/10.1016/0040-1951(89)90338-7)
- Storey, B. C., & Dalziel, I. W. (1987). Outline of the structural and tectonic history of the Ellsworth Mountains-Thiel Mountains Ridge, West Antarctica. In G. D. McKenzie (Ed.), *Gondwana Six: Structure, Tectonics, and Geophysics* (pp. 117–128). <https://doi.org/10.1029/GM040p0117>
- Storey, B., & Kyle, P. (1997). An active mantle mechanism for Gondwana breakup. *South African Journal of Geology*, 100(4), 283–290.
- Tatham, D. J., Lloyd, G. E., Butler, R. W. H., & Casey, M. (2008). Amphibole and lower crustal seismic properties. *Earth and Planetary Science Letters*, 267(1), 118–128. <https://doi.org/10.1016/j.epsl.2007.11.042>
- Wannamaker, P., Hill, G., Stodt, J., Maris, V., Ogawa, Y., Selway, K., et al. (2017). Uplift of the central Transantarctic Mountains. *Nature Communications*, 8(1), 1588.
- Weiss, T., Siegesmund, S., Rabbal, W., Bohlen, T., & Pohl, M. (1999). Seismic velocities and anisotropy of the lower continental crust: A review. *Pure and Applied Geophysics*, 156(1), 97–122. <https://doi.org/10.1007/s000240050291>
- Wessel, P., & Smith, W. H. F. (1998). New, improved version of the Generic Mapping Tools released. *Eos, Transactions American Geophysical Union*, 79(579), 579–579.
- Winberry, J. P., & Anandakrishnan, S. (2004). Crustal structure of the West Antarctic rift system and Marie Byrd Land hotspot. *Geology*, 32(11), 977–980. <https://doi.org/10.1130/G20768.1>
- Wysoczanski, R. J., Gamble, J. A., Kyle, P. R., & Thirlwall, M. F. (1995). The petrology of lower crustal xenoliths from the Executive Committee Range, Marie Byrd Land Volcanic Province, West Antarctica. *Lithos*, 36(3), 185–201. [https://doi.org/10.1016/0024-4937\(95\)00017-8](https://doi.org/10.1016/0024-4937(95)00017-8)
- Yang, Y., & Ritzwoller, M. H. (2008). Characteristics of ambient seismic noise as a source for surface wave tomography. *Geochemistry, Geophysics, Geosystems*, 9, Q02008. <https://doi.org/10.1029/2007GC001814>